# A Simulation-Based Error Budget of the TES Method for the Design of the Spectral Configuration of the Micro-Bolometer-Based MISTIGRI Thermal Infrared Sensor

Frédéric Jacob, *Senior Member, IEEE*, Thomas H. G. Vidal, Audrey Lesaignoux, Albert Olioso, Marie Weiss, Françoise Nerry, Stéphane Jacquemoud, Philippe Gamet, Karine Caillault, Luc Labarre, Andrew French, *Member, IEEE*, Thomas Schmugge, *Fellow, IEEE*, Xavier Briottet, and Jean-Pierre Lagouarde

***Abstract*— In preparation of the micro-bolometer-based MIcro Satellite for Thermal Infrared GRound surface Imaging (MISTIGRI) mission, we study the error budget of the Temperature-Emissivity Separation (TES) method using several spectral configurations that differ in channel numbers, locations, and widths. The error budget quantifies the contribution of 1) the TES underlying assumption about emissivity spectral contrast, 2) the errors on atmospheric corrections, and 3) the instrumental noise. When dealing with atmospheric corrections, we consider errors in atmospheric temperature, water vapor content, and concentrations of $CO_2$ and $O_3$. To that end, we design an end-to-end simulator of MISTIGRI measurements in order to simulate the radiative and biophysical quantities involved in the data processing. We conduct numerous simulations over a wide range of realistic setups that include cavity effect, i.e., radiance trapping within vegetation canopy. In the case of micro-bolometer-based sensing, the current study highlights that atmospheric and instrumental noises have similar impacts on the TES retrievals, with resulting errors twice as large as those due to the TES intrinsic assumption about spectral contrast, where the latter contributes to the TES error budget within the [0.005–0.009] interval for emissivity, and within the [0.3–0.4 K] interval for land surface temperature (LST). Also, we show that retrieval performance of surface temperature is very similar across all considered MISTIGRI spectral configurations, with RMSE variation within 0.2 K. Eventually, our study permits us to select a 4-channels spectral configuration as the most suited for the MISTIGRI instrument, notably because it enables a moderately better capture of the emissivity contrast than a 3-channels one.**

***Index Terms*— Atmospheric corrections, micro-bolometers detectors, satellite mission design, temperature emissivity separation (TES) error budget, temperature/emissivity separation, thermal infrared remote sensing, vegetation canopy-scaled cavity effects.**

## I. Introduction

THERMAL InfraRed (TIR) remote sensing is a powerful tool for Earth system monitoring, since it provides proxies of Earth surface emissivity spectrum/radiometric temperature that are widely used in several thematic studies. Involved processes are related to radiation budget [1]–[5], land surface energy balance and evapotranspiration [6]–[15], soil moisture and vegetation water status [16]–[18], crop micro-meteorological conditions [19], urban heat island and urban atmospheric flows [20]–[22], volcanic ashes with sulfate and sulfur dioxide deposits [23], [24], lava flow monitoring and modeling [25], [26], mineral mapping [27], [28], cryospheric inventory and worldwide glacier balance [29], [30], as well as numerical weather prediction and ocean forecasting modeling [31], [32]. Various satellite TIR missions have been dedicated to the estimation of land surface temperature (LST) during the last three decades, either with high spatial resolution sensors such as Landsat [33], [34] and advanced spaceborne thermal emission and reflection radiometer (ASTER) [7], [35], [36], or with high temporal resolution sensors such as advanced very high-resolution radiometer (AVHRR) [37], [38], météosat seconde génération (MSG) [39], [40], moderate-resolution imaging spectroradiometer (MODIS) [41], [42], or sea and LST radiometer (SLSTR) onboard Sentinel 3 [31], [43]. Although disaggregation approaches have been explored to overcome the lack

Manuscript received April 13, 2021; revised June 29, 2021; accepted July 19, 2021. This work was supported by the French Space Agency through CNES in the context of the preparation of the MISTIGRI Mission under Contract 104075. *(Corresponding author: Thomas H. G. Vidal.)*

Frédéric Jacob and Audrey Lesaignoux are with UMR LISAH, IRD, INRAE, Institut Agro-Montpellier SupAgro, University of Montpellier, 34060 Montpellier, France (e-mail: frederic.jacob@ird.fr; alesaignoux@gmail.com).

Thomas H. G. Vidal is with ACRI-ST, 31000 Toulouse, France (e-mail: thomas.vidal@acri-st.fr).

Albert Olioso and Marie Weiss are with EMMAH, INRAE, Avignon Université, 84000 Avignon, France (e-mail: albert.olioso@inrae.fr; marie.weiss@inrae.fr).

Françoise Nerry is with ICube, Université de Strasbourg, CNRS, 67412 Illkirch, France (e-mail: f.nerry@unistra.fr).

Stéphane Jacquemoud is with Université de Paris, IPGP, CNRS, F-75005 Paris, France (e-mail: jacquemoud@ipgp.fr).

Philippe Gamet is with French Space Agency (CNES), Center d'Etudes Spatiales de la BIOsphere (CESBIO), Université de Toulouse, 31401 Toulouse, France (e-mail: philippe.gamet@cnes.fr).

Karine Caillault and Luc Labarre are with ONERA/DOTA, Université Paris Saclay, F-91123 Palaiseau, France (e-mail: karine.caillault@onera.fr; luc.labarre@onera.fr).

Andrew French is with USDA/ARS/ALARC, Maricopa, AZ 85238 USA (e-mail: andrew.french@ars.usda.gov).

Thomas Schmugge is with NM Water Resources Institute, NMSU, Las Cruces, NM 88003 USA (e-mail: schmugge@nmsu.edu).

Xavier Briottet is with ONERA-DOTA, University of Toulouse, FR-31055 Toulouse, France (e-mail: xavier.briottet@onera.fr).

Jean-Pierre Lagouarde is with INRAE/UMR ISPA, 33882 Villenave d'Ornon, France (e-mail: jean-pierre.lagouarde@inra.fr).

Digital Object Identifier 10.1109/TGRS.2021.3099896

of TIR data with both high spatial and temporal resolutions [44], [45], several studies have campaigned for satellite missions providing such TIR data, including Infra Red miniSatellite Unit for Terrestrial Environment (IRSUTE) [46], SPECTRA [47], ECOsystem Spaceborne Thermal Radiometer Experiment on Space Station (ECOSTRESS) [48], or LST monitoring (LSTM) [49].

The MIcro Satellite for Thermal Infrared GRound surface Imaging (MISTIGRI) preparatory mission was initiated and conducted by CNES (French space agency) in collaboration with Spain, between 2010 and 2015 [50]. Follow-on from IRSUTE and SPECTRA, it was the precursor of the TIR Imaging Satellite for High-resolution Natural resource Assessment (TRISHNA) mission, to be launched in 2025 [51]. The primary objective of the MISTIGRI mission was the monitoring of land surface energy and water budgets. The spatial resolution was set to 50 m, and the revisiting rate was set to one day, with an overpass within the [12:00–13:00] solar time interval. The one-day revisit induced a constant off-nadir viewing with a view zenith angle lower than 40°. Finally, the MISTIGRI instrument was designed with micro-bolometer sensors, which led to a set of large spectral channels for reducing instrumental noise, whose expected values were between 0.2 and 0.5 K at 290 K. The baseline instrument spectral configuration included 4 channels labeled TIR3, TIR4, TIR1, and TIR2, respectively, centered at 8.6 $\mu$m (0.32 $\mu$m width), 9.1 $\mu$m (0.32 $\mu$m width), 10.3 $\mu$m (1.02 $\mu$m width), and 11.5 $\mu$m (1.02 $\mu$m width).

Retrieving surface emissivity and temperature from TIR remote sensor measurements is an ill-posed problem, with $N_b$ equations from channel measurements and $N_b + 1$ unknowns that include $N_b$ channel emissivities and one radiometric temperature. Among the existing solutions that consist in adding an $N_b + 1$ equation to the system [52]–[54], we chose the Temperature Emissivity Separation method (TES, [35], [55]). This choice is motivated by the TES capability to retrieve surface emissivity and temperature from a unique multispectral snapshot at the satellite overpass time, thus making possible the monitoring of temporal changes of surface temperature on the basis of a one-day revisiting rate. The TES method relies on the assumption that any natural surface emissivity spectrum includes a value close to unity within the TIR spectral range, which induces the possibility to derive the emissivity minimum value from emissivity contrast by using an empirical relationship [56], [57]. The TES method has been extensively used and studied in the past three decades, notably in order to enhance its stability and performance, with regard to observation conditions driven by sensor capabilities, atmospheric conditions and land surface spectral properties [1], [3], [36], [55]–[75].

When designing any satellite mission, an important step is the definition of the mission characteristics in accordance with the approaches that are used for data processing and thematic uses. As overviewed in [50] for the MISTIGRI mission, some instances are the revisiting rate/overpass time in the light of evapotranspiration diurnal course or the viewing direction in the light of radiative transfer processes. In the context of monitoring LST, the definition of the spectral configuration of the MISTIGRI sensor has to be investigated with regards to sensor technologies (i.e., micro-bolometers detectors) and used methods (e.g., TES retrieval of emissivity/temperature with prior atmospheric corrections). More particularly, the appropriate locations and widths for the MISTIGRI spectral channels should balance between three constraints: capturing spectral contrasts of the observed emissivity spectra, minimizing atmospheric perturbations, and minimizing instrumental noise.

The current study aims to conduct an error budget for the TES method when used over MISTIGRI imagery of vegetated land surfaces (mission primary objective), in order to find an appropriate sensor spectral configuration among predefined configurations, on the basis of balancing between the three aforementioned constraints. To that end, an end-to-end simulator is implemented, which is dedicated to: 1) the simulation of TIR multispectral measurements and 2) use of the TES method for LST retrieval after prerequisite atmospheric corrections. The simulator relies on simulated land surface emissivity spectra that account for radiance trapping within vegetation canopy since [57] showed that the subsequent cavity effect induces an upper shift of emissivity for both the TES empirical relationship and the subsequent retrievals. We first detail the process flow of both the TES method and the end-to-end simulator in § II and § III, respectively. Next, we present the simulator implementation in § IV, and the simulation strategy when addressing the MISTIGRI mission in § V. We finally present and discuss our results in § VI, and we conclude with current limitations and further perspectives in § VII.

## II. TES Presentation

### A. TES Principle and Overview

Rather than associating the maximum emissivity with a nominal value [76], the TES approach assumes that the emissivity spectrum of a natural surface in the TIR spectral domain includes a maximum value bounded within the [0.98–1] interval. Subsequently, any change in the emissivity spectrum minimum value is related to a change in the spectral contrast across the emissivity spectrum [57]. Thus, by empirically relating the minimum emissivity to the spectral dynamics observed across the $N_b$ channels [68], TES overcomes the indetermination by removing the $(N_b + 1)$th unknown of the ill-posed problem for LST retrieval (see § I). To that end, channel emissivities and radiometric temperature are retrieved via an iterative process that includes four steps described below.

### B. TES Processing Flow

The first step estimates radiometric surface temperature $T_R^{\text{sur}}$ as the maximum temperature over the $N_b$ channels $j$

$$T_R^{\text{sur}} = \max\left(T_j\right) \tag{1}$$

where radiometric temperature $T_j$ for channel $j$ is deduced via the inverse Planck's law $L_{\text{BB}}^{-1}$ applied to the corresponding surface-emitted radiance $L_j^{\text{em}}$, itself derived from measured surface outgoing radiance $L_j^{\text{sur}\uparrow}$ after atmospheric corrections, and from atmospheric downwelling irradiance $E_j^{\text{atm}\downarrow}$

$$L_j^{\text{em}} = L_j^{\text{sur}\uparrow} - \left(1 - \varepsilon_j\right)\frac{E_j^{\text{atm}\downarrow}}{\pi} \tag{2}$$

$$T_j = L_{\text{BB}}^{-1}\left(\frac{L_j^{\text{em}}}{\varepsilon_j}, \lambda_j\right) \tag{3}$$

$$L_{\mathrm{BB}}^{-1}(L_j, \lambda_j) = c_2 \left[ \lambda_j \ln\left( \frac{c_1}{\pi \lambda_j^5 L_j} + 1 \right) \right]^{-1} \quad (4)$$

with $c_1$ and $c_2$ the first and second radiation constants, equal to $3.74151.10^{-16}$ W.m$^{-2}$ and 0.0143879 m.K, respectively. $\varepsilon_j$ and $\lambda_j$ are channel emissivity and central wavelength, respectively.

The second step is the calculation of relative emissivities as the ratios of channel emissivities $\varepsilon_j$ to the mean emissivity over the $N_b$ channels

$$\beta_j = \frac{\varepsilon_j}{\langle \varepsilon_j \rangle} = \frac{L_j^{\mathrm{em}} / L_{\mathrm{BB}}\left(T_R^{\mathrm{sur}}, \lambda_j\right)}{\left\langle L_j^{\mathrm{em}} / L_{\mathrm{BB}}\left(T_R^{\mathrm{sur}}, \lambda_j\right) \right\rangle} \quad (5)$$

where $L_{\mathrm{BB}}$ is the Planck's law

$$L_{\mathrm{BB}}\left(T_R^{\mathrm{sur}}, \lambda_j\right) = c_1 \left[ \lambda_j^5 \pi \left[ \exp\left( \frac{c_2}{\lambda_j T_R^{\mathrm{sur}}} \right) - 1 \right] \right]^{-1}. \quad (6)$$

The third step consists of calculating the minimum value of the emissivity spectrum as an empirical relationship of the Maximum Minimum Difference (MMD $\equiv$ spectral contrast) of the relative emissivities $\beta_j$

$$\mathrm{MMD} = \beta_{\max} - \beta_{\min} = \frac{\max(\varepsilon_j) - \min(\varepsilon_j)}{\langle \varepsilon_j \rangle} \quad (7)$$

$$\varepsilon_{\min} = A + B \times \mathrm{MMD}^C \quad (8)$$

where $A$, $B$, and $C$ are coefficients that depend on the spectral configuration of the instrument, and which are estimated from nonlinear regression over a database of emissivity spectra (see details in [57]).

In the fourth and last step, the channel emissivities over the $N_b$ channels are derived from the minimum channel emissivity value as

$$\varepsilon_j = \frac{\varepsilon_{\min}}{\beta_{\min}} \beta_j. \quad (9)$$

The TES iterative process is initialized by setting to unity the emissivity values $\varepsilon_j$ in (2) for each channel $j$ (radiometric temperature is set to brightness temperature). From this initialization, the iterative procedure follows (1)–(9). For our study, we set a maximum of ten iterations, but the process systematically converges in fewer than six iterations. Once convergence is reached, TES retrievals of both channel emissivity TES-$\varepsilon_j$ over the $N_b$ channels and radiometric temperature surface TES-$T_R^{\mathrm{sur}}$ are obtained from the last iteration on (9) and (1), respectively.

## III. SiMi Description

### A. SiMi Overview

The specification of the optimal MISTIGRI spectral configuration is performed using simulated data. The simulator for MISTIGRI measurements (SiMi) is designed, on a single pixel basis, 1/ to simulate radiative transfer processes involved in TIR data measurements along with related quantities, and 2/ to analyze the performance of the retrieval procedure for the variables of interest, including atmospheric corrections and recovering of land surface emissivity/temperature with the TES method. The simulations cover the TIR spectral range ([7.5–13.5] $\mu$m) with a $10^{-3}$ $\mu$m resolution. SiMi includes five connected modules illustrated in Fig. 1 and described below (quantities mentioned in Fig. 1 are defined in Table I).

1) The synthetic scene module (Module 1) describes the scene at the land surface level, by considering an equivalent homogeneous body with the same radiative characteristics, namely emissivity spectrum and radiometric temperature, than the actual composite of plant canopy and underlying soil [77].
2) The atmosphere module (Module 2) is dedicated to the simulation of atmospheric effects on the measured signal. On the basis of predefined atmospheric conditions, it simulates the atmospheric radiative transfer and the resulting signal at the sensor input top of the atmosphere (TOA), and it quantifies the atmospheric radiative quantities to be used for atmospheric corrections.
3) The instrument module (Module 3a) computes the quantities measured by the instrument (channel radiances/brightness temperatures) in accordance with spectral response function and instrumental noise for each channel.
4) The calibration module (Module 3b) deals with the calibration of the TES empirical relationship $\varepsilon_{\min} = f(\mathrm{MMD})$ (8). This relationship depends upon the channel locations and widths, and has to be calibrated for each spectral configuration [57].
5) The inversion module (Module 4) performs the inversion of the simulated measurements. It first applies atmospheric corrections and then makes use of the TES method to separate target emissivity and temperature.

### B. Land Surface Module (Module 1)

The land surface module generates emissivity spectra for a given scene consisting of vegetation canopy and underlying soil, using the Scattering by Arbitrarily Inclined Leaves-Thermique (SAIL-Thermique) radiative transfer model [78], [79]. It describes land surface as a turbid medium, with a stack of homogeneous vegetation layers above a soil substrate. Vegetation canopy is characterized by canopy structure [i.e., leaf area index (LAI) and leaf inclination distribution function average leaf angle (ALA)] and leaf optical properties (reflectance and transmittance spectra). The underlying soil surface is characterized by optical properties (soil reflectance spectra). Radiative transfer is simulated by accounting for successive scattering within the canopy, and between the canopy and the soil. SAIL-Thermique considers the Kirchhoff's law at the thermodynamical equilibrium, where directional surface emissivity $\varepsilon_\lambda$ is calculated from the directional-hemispherical reflectance $\rho_\lambda$: $\varepsilon_\lambda = 1 - \rho_\lambda$. SAIL-Thermique is used to generate two datasets.

1) The first dataset, called DB1, is used to compute the spectral surface leaving radiance $L_\lambda^{\mathrm{sur}\uparrow}$, by combining any emissivity spectrum $\varepsilon_\lambda$ with prescribed values of surface radiometric temperature $T_R^{\mathrm{sur}}$. Each pair {$\varepsilon_\lambda$ spectrum, $T_R^{\mathrm{sur}}$ value} corresponds to a land surface scene. This pair is provided to Module 2, and further serves as a reference for validation exercises. The first exercise consists in validating the TES semi-empirical relationship, once calibrated. The second

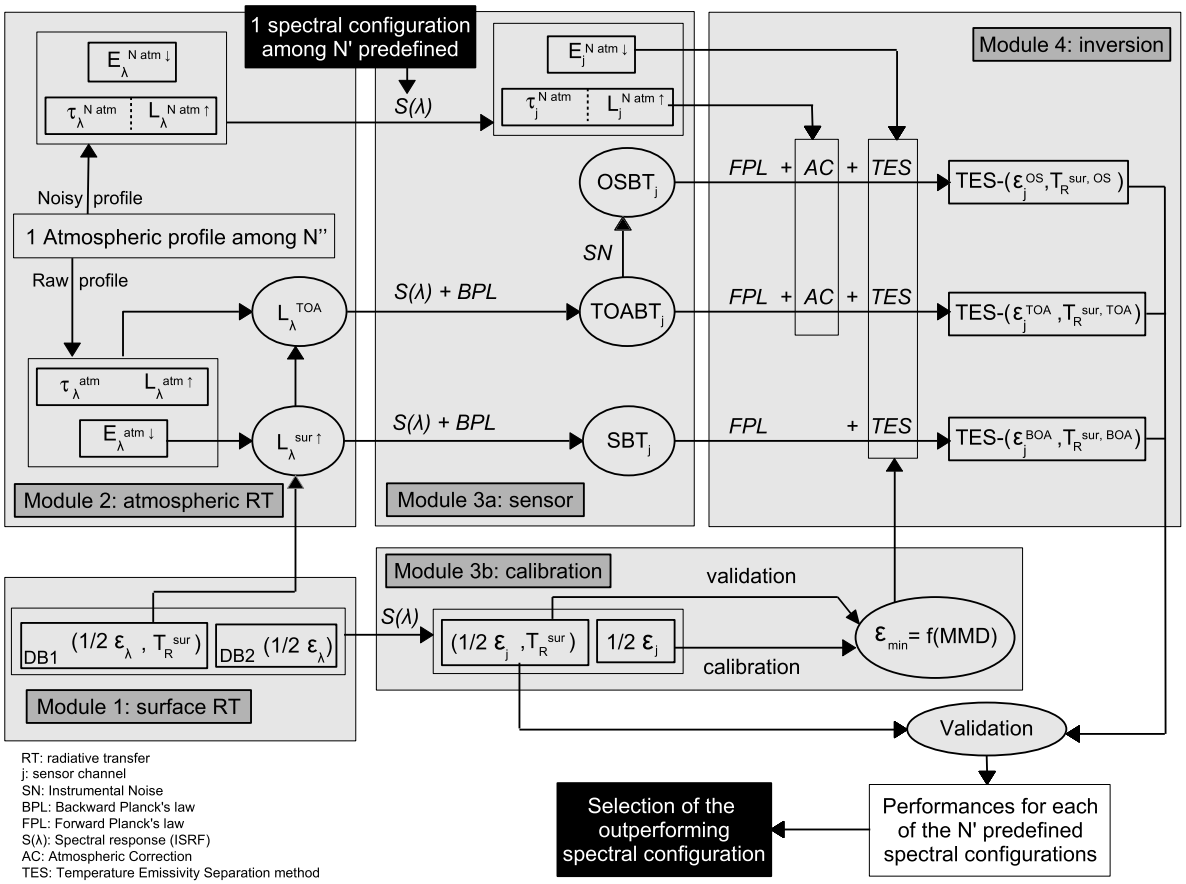


Fig. 1. Overview of the approach used to identify an optimal spectral configuration in the TIR range for the MISTIGRI instrument. Quantities mentioned in the Figure are defined in Table I.

exercise consists in validating TES retrievals of channel emissivity and radiometric temperature (Fig. 1).

2) The second dataset, called DB2, is used to calibrate the TES semi-empirical relationship (Module 3b).

### C. Atmosphere Module (Module 2)

For any pair {$\varepsilon_\lambda$ spectrum, $T_R^{\text{sur}}$ value}, the atmosphere module computes several spectral quantities: atmospheric downwelling irradiance $E_\lambda^{\text{atm}\downarrow}$, surface-leaving radiance $L_\lambda^{\text{sur}\uparrow}$ (10) and (11), atmospheric transmittance $\tau_\lambda^{\text{atm}}$, atmospheric upwelling radiance at the sensor level $L_\lambda^{\text{atm}\uparrow}$, and TOA radiance at the sensor entrance $L_\lambda^{\text{TOA}}$ (12)

$$L_\lambda^{\text{sur}\uparrow} = L_\lambda^{\text{em}} + (1-\varepsilon_\lambda)\frac{E_\lambda^{\text{atm}\downarrow}}{\pi} \tag{10}$$

$$L_\lambda^{\text{em}} = \varepsilon_\lambda L_{\text{BB}}\left(T_R^{\text{sur}}, \lambda\right) \tag{11}$$

$$L_\lambda^{\text{TOA}} = \tau_\lambda^{\text{atm}} L_\lambda^{\text{sur}\uparrow} + L_\lambda^{\text{atm}\uparrow}. \tag{12}$$

The calculations of $E_\lambda^{\text{atm}\downarrow}$, $\tau_\lambda^{\text{atm}}$, and $L_\lambda^{\text{atm}\uparrow}$ involve the simulation of atmospheric radiative transfer based on atmospheric profiles of pressure, temperature, humidity, as well as of concentrations in carbon dioxide [$CO_2$] and ozone [$O_3$] [80], [81]. The radiative transfer is simulated using the modélisation avancée de la terre pour l'imagerie et la simulation des scénes et de leur environnement (MATISSE)-v2 code [82], [83]. MATISSE is chosen for its consistent atmospheric profile database, given that it is very similar to its counterparts such as MODerate resolution atmospheric TRANsmission (MODTRAN) for radiative transfer simulation. After these calculations, each atmospheric profile is characterized by a triplet $\{E_\lambda^{\text{atm}\downarrow}, \tau_\lambda^{\text{atm}}, L_\lambda^{\text{atm}\uparrow}\}$, to be combined with each pair {$\varepsilon_\lambda$ spectrum, $T_R^{\text{sur}}$ value}.

The atmosphere module also computes the atmospheric radiative quantities, namely $E_\lambda^{N\,\text{atm}\downarrow}$, $\tau_\lambda^{N\,\text{atm}}$, and $L_\lambda^{N\,\text{atm}\uparrow}$, to be used for atmospheric corrections in Module 4 after convolution with the instrumental spectral response function (ISRF) in Module 3a (Fig. 1). To that end, and in order to account for errors on atmospheric corrections due to partial knowledge on atmospheric status, atmospheric profiles are noised on temperature $T_{\text{atm}}(z)$ and humidity hr($z$), as well as on concentrations of carbon dioxide [$CO_2$]($z$) and ozone [$O_3$]($z$), where $z$ is the altitude above sea level. Each variable profile Var($z$) is noised using a Gaussian white noise

$$\text{Var}(z) = \text{Var}(z) + \mathcal{N}(0; \alpha.\text{Var}(z) + \beta) \tag{13}$$

$$\text{Var}(z) \in \{T_{\text{atm}}(z), \text{hr}(z), [CO_2](z), [O_3](z)\} \tag{14}$$

where $\alpha$ and $\beta$ are set up as follows:

1) in accordance with [84], we set a standard deviation of 0.8 K for $T_{\text{atm}}(z)$ ($\alpha = 0$, $\beta = 0.8$), which corresponds to a maximum error of 2 K;

TABLE I
SIGNIFICATION OF THE RADIATIVE QUANTITIES THAT ARE MENTIONED IN FIG. 1

| Parameters | Description |
|---|---|
| $\varepsilon_\lambda$ | Spectral land surface emissivity |
| $\varepsilon_j$ | Channel land surface emissivity |
| $\varepsilon_{min}$ | Minimum value of $\varepsilon_j$ across $N_b$ channels |
| $MMD$ | Maximum-Minimum Difference (Equation 7) |
| $T_R^{sur}$ | Land surface radiometric temperature |
| $E_\lambda^{atm\downarrow}$ | Spectral atmospheric downwelling irradiance |
| $E_\lambda^{N,atm\downarrow}$ | Noised spectral atmospheric downwelling irradiance (1) |
| $E_j^{atm\downarrow}$ | Channel atmospheric downwelling irradiance |
| $E_j^{N,atm\downarrow}$ | Noised channel atmospheric downwelling irradiance (1) |
| $\tau_\lambda^{atm}$ | Spectral atmospheric transmittance |
| $\tau_\lambda^{N,atm}$ | Noised spectral atmospheric transmittance (1) |
| $\tau_j^{atm}$ | Channel atmospheric transmittance |
| $\tau_j^{N,atm}$ | Noised channel atmospheric transmittance (1) |
| $L_\lambda^{atm\uparrow}$ | Spectral atmospheric upwelling radiance |
| $L_\lambda^{N,atm\uparrow}$ | Noised spectral atmospheric upwelling radiance (1) |
| $L_j^{atm\uparrow}$ | Channel atmospheric upwelling radiance |
| $L_j^{N,atm\uparrow}$ | Noised channel atmospheric upwelling radiance (1) |
| $L_\lambda^{sur\uparrow}$ | Spectral surface leaving radiance |
| $L_j^{sur\uparrow}$ | Channel surface leaving radiance |
| $L_\lambda^{TOA\uparrow}$ | Spectral top of atmosphere radiance |
| $L_j^{TOA\uparrow}$ | Channel top of atmosphere radiance |
| $\mathrm{SBT}_j$ | Surface brightness temperature |
| $\mathrm{TOABT}_j$ | Top-of-atmosphere brightness temperature |
| $\mathrm{OSBT}_j$ | Out-of-sensor brightness temperature |
| $TES-(\varepsilon_j^{BOA}, T_R^{sur,BOA})$ | TES retrievals of emissivity / temperature from SBT$j$ |
| $TES-(\varepsilon_j^{TOA}, T_R^{sur,TOA})$ | TES retrievals of emissivity / temperature from $\mathrm{TOABT}_j$ |
| $TES-(\varepsilon_j^{OS}, T_R^{sur,OS})$ | TES retrievals of emissivity / temperature from OSBT$j$ |
| (1) from noised atmospheric profile to account for uncertainties on atmospheric status | |

2) in accordance with [85] and [84], we set a standard deviation of $0.1 \times \mathrm{hr}(z)$ for $\mathrm{hr}(z)$ ($\alpha = 0.1$, $\beta = 0$), which corresponds to a maximum relative error of 25%;
3) in accordance with [81], we set a standard deviation of $0.15 \times [CO_2](z)$ for $[CO_2](z)$ ($\alpha = 0.15$, $\beta = 0$), which corresponds to a maximum relative error of 40%;
4) In accordance with [85], we set a standard deviation of $0.2 \times [O_3](z)$ on $[O_3](z)$ ($\alpha = 0.2$, $\beta = 0$), which corresponds to a maximum relative error of 50%.

### *D. Instrument Module (Module 3a)*

The instrument module accounts for the sensitivity of each spectral channel, and for the associated Noise Equivalent Difference Temperature (NEDT) that depends upon channel width.

To account for sensitivity of channel $j$, any spectrum (e.g., emissivity, radiance, transmittance) $Q_\lambda$ is convolved with the dedicated ISRF that spreads over the $[\lambda_{\min,j} - \lambda_{\max,j}]$ interval, thus providing the waveband equivalent value $Q_j$

$$Q_j = \frac{\int_{\lambda_{\min,j}}^{\lambda_{\max,j}} Q_\lambda S_j(\lambda) \mathrm{d}\lambda}{\int_{\lambda_{\min,j}}^{\lambda_{\max,j}} S_j(\lambda) \mathrm{d}\lambda}. \quad (15)$$

Accounting for instrumental noise on measured temperature consists of adding, for any channel $j$, a Gaussian white noise with a standard deviation equal to the corresponding $\mathrm{NEDT}_j$

$$\mathrm{OSBT}_j = \mathrm{BT}_j + \mathcal{N}\big(0, \mathrm{NEDT}_j\big) \quad (16)$$

where $\mathrm{BT}_j$ is the brightness temperature at the sensor level, and out of sensor brightness temperaturen $(\mathrm{OSBT})_j$ is the output sensor (OS) brightness temperature with instrumental noise. NEDT$j$ is provided by the sensor manufacturer as a function of both measured brightness temperature and channel width (full-width at half-maximum, FWHM).

In the context of satellite mission design, it is valuable to characterize the error budget at different levels. To that end, Module 3a provides estimates of measured brightness temperatures over the $N_b$ channels $j$ for three different cases of $\mathrm{BT}_j$ (Fig. 1):

1) $\mathrm{SBT}_j$ corresponds to brightness temperatures at the surface level, it is derived from radiance spectrum $L_\lambda^{\mathrm{sur}\uparrow}$;
2) top-of-atmosphere brightness temperature $(\mathrm{TOABT})_j$ corresponds to brightness temperatures at the satellite level above the atmosphere, it is derived from radiance spectrum $L_\lambda^{\mathrm{TOA}}$;
3) $\mathrm{OSBT}_j$ is derived from $\mathrm{TOABT}_j$ by applying the Gaussian white noise formulation (16).

Note that both $\mathrm{SBT}_j$ and $\mathrm{TOABT}_j$ are derived from corresponding radiances after convolution with the dedicated ISRF and application of the inverse Planck's Law $L_{\mathrm{BB}}^{-1}$ (4).

### E. Calibration Module (Module 3b)

The calibration module aims to calibrate the TES empirical relationship $\varepsilon_{\min} = f(\text{MMD})$ that derives minimum emissivity from the spectral contrast captured by multispectral TIR measurements over $N_b$ channels. To that end, emissivity minimum and maximum values, as well as MMD (7), are derived for each emissivity spectrum from DB2 database, after convolution with ISRF $S(\lambda)$ (15).

The calibration is performed by computing the empirical coefficients $A$, $B$ and $C$ of the $\varepsilon_{\min} = f(\text{MMD})$ relationship (8) using the "Optim" R function [86]. The latter minimizes the calibration residual error expressed as the root mean square error $(\text{RMSE})_{\text{cal}}^{\varepsilon_{\min}}$ [87]

$$\text{RMSE}_{\text{cal}}^{\varepsilon_{\min}} = \sqrt{\frac{\sum_{n2}\left(\varepsilon_{\min}^{\text{obs-cal}} - \varepsilon_{\min}^{\text{est}}\right)^2}{n2}} \tag{17}$$

where $\varepsilon_{\min}^{\text{obs-cal}}$ and $\varepsilon_{\min}^{\text{est}}$ are, respectively, the $\varepsilon_{\min}$ reference values from the DB2 subset of emissivity spectra and the $\varepsilon_{\min}$ estimates from (8) with the calibrated coefficients, and $n2$ is the number of emissivity spectra within the DB2 subset:

The validation of the calibrated empirical relationship is conducted using the DB1 subset of emissivity spectra, by computing $\text{RMSE}_{\text{val}}^{\varepsilon_{\min}}$ as

$$\text{RMSE}_{\text{val}}^{\varepsilon_{\min}} = \sqrt{\frac{\sum_{n1}\left(\varepsilon_{\min}^{\text{obs-val}} - \varepsilon_{\min}^{\text{est}}\right)^2}{n1}} \tag{18}$$

where $\varepsilon_{\min}^{\text{obs-val}}$ are the $\varepsilon_{\min}$ reference values from DB1 subset of emissivity spectra, and $n1$ is the number of emissivity spectra within the DB1 subset.

### F. Inversion Module (Module 4)

The inversion module aims to retrieve land surface emissivity and radiometric temperature from the MISTIGRI simulated measurements. It first corrects sensor data from atmospheric perturbations, and second applies the TES method to retrieve emissivity $\varepsilon_j$ over the $N_b$ channels $j$ along with the associated radiometric surface temperature $T_R^{\text{sur}}$ (see Fig. 1).

Upon entry in the inversion module, brightness temperatures from Module 3a are converted into channel radiances by using the Planck's law $L_{\text{BB}}$ (6). Atmospheric corrections are then performed using the noised atmospheric radiative quantities that are computed from noised atmospheric profiles in Module 2 and next ISRF-convolved in Module 3a, namely the noised channel atmospheric transmittance $\tau_j^{N\,\text{atm}}$ and the noised upwelling radiance at the sensor level $L_j^{N\,\text{atm}\uparrow}$

$$L_j^{\text{sur}\uparrow} = \frac{L_j^{\text{OS}} - L_j^{N\,\text{atm}\uparrow}}{\tau_j^{N\,\text{atm}}} \tag{19}$$

where $L_j^{\text{OS}}$ and $L_j^{\text{sur}\uparrow}$ are the radiances over channel $j$ at the sensor level (before atmospheric corrections) and at the surface level (after atmospheric corrections), respectively.

Afterward, the TES method is applied on the channel radiances at the surface level $L_j^{\text{sur}\uparrow}$, by using the ISRF-convolved values of noised atmospheric downwelling irradiance $E_j^{N\,\text{atm}\downarrow}$ [see Fig. 1 and (2)]. As explained in Section III-D, it is valuable to characterize the error budget at different levels, in the context of satellite mission design. To that end, SiMi permits to apply the inversion procedure at three levels (Fig. 1):

1) applying the TES method on sensor measurements of surface brightness temperature at the surface level, so-called $\text{SBT}_j$, to quantify errors resulting from TES assumptions only;
2) applying atmospheric corrections and the TES method on TOA brightness temperature at the sensor level, so-called $\text{TOABT}_j$, to quantify errors resulting from both atmospheric perturbations and TES assumptions;
3) applying atmospheric corrections and the TES method on OS brightness temperature, so-called $\text{OSBT}_j$, to quantify errors resulting from instrumental noise, atmospheric perturbations, and TES assumptions.

Thus, TES retrieves the pairs $\{\text{TES-}\varepsilon_j^{\text{BOA}}, \text{TES-}T_R^{\text{sur,BOA}}\}$ from $\text{SBT}_j$ (BOA stands for bottom of atmosphere), $\{\text{TES-}\varepsilon_j^{\text{TOA}}, \text{TES-}T_R^{\text{sur,TOA}}\}$ from $\text{TOABT}_j$ (TOA stands for top of atmosphere), and $\{\text{TES-}\varepsilon_j^{\text{OS}}, \text{TES-}T_R^{\text{sur,OS}}\}$ from $\text{OSBT}_j$ (OS stands for out of sensor), where each pair corresponds to each of the three aforementioned cases, respectively.

### G. Performance Analysis

For each spectral configuration characterized by a set of $N_b$ channels with the corresponding ISRF $S_j(\lambda)$, the TES retrievals of surface emissivities and temperatures are compared with their initial counterparts at the simulator entrance (see Fig. 1). For emissivity, these counterparts are the ISRF-convolved values of the emissivity spectra $\varepsilon_\lambda$ within the DB1 subset. The comparison is based on the quantification of RMSE values between the initial counterparts $(\varepsilon_j,\ T_R^{\text{sur}})$ and their corresponding values for the three types of product considered $(\text{TES-}\varepsilon_j^k,\ \text{TES-}T_R^{\text{sur},k})_{k\in\{\text{BOA,TOA,OS}\}}$

$$\text{RMSE}_{\varepsilon_j^k}^{\text{TES}} = \sqrt{\frac{\sum_{N_{\text{ret}}}\left(\text{TES-}\varepsilon_j^k - \varepsilon_j\right)^2}{N_{\text{ret}}}} \tag{20}$$

$$\text{RMSE}_{T_R^{\text{sur},k}}^{\text{TES}} = \sqrt{\frac{\sum_{N_{\text{ret}}}\left(\text{TES-}T_R^{\text{sur},k} - T_R^{\text{sur}}\right)^2}{N_{\text{ret}}}} \tag{21}$$

where $N_{\text{ret}}$ is the number of retrievals considered in each case.

## IV. SiMi Implementation

Once the SiMi simulator is designed, the next step is implementation. This consists of providing ancillary information in order to document land surface and atmospheric conditions.

### A. Database for Land Surface Emissivity

We select for the current study the emissivity dataset computed with Module 1 in the framework of a previous study that evaluated the impact of vegetation cavity effect on the performance of the TES method [57]. The resulting dataset includes simulated emissivity spectra for a panel of soil/vegetation canopy combinations, which provides a representative dataset for satellite mission design. By considering a large range of inputs related to vegetation canopy

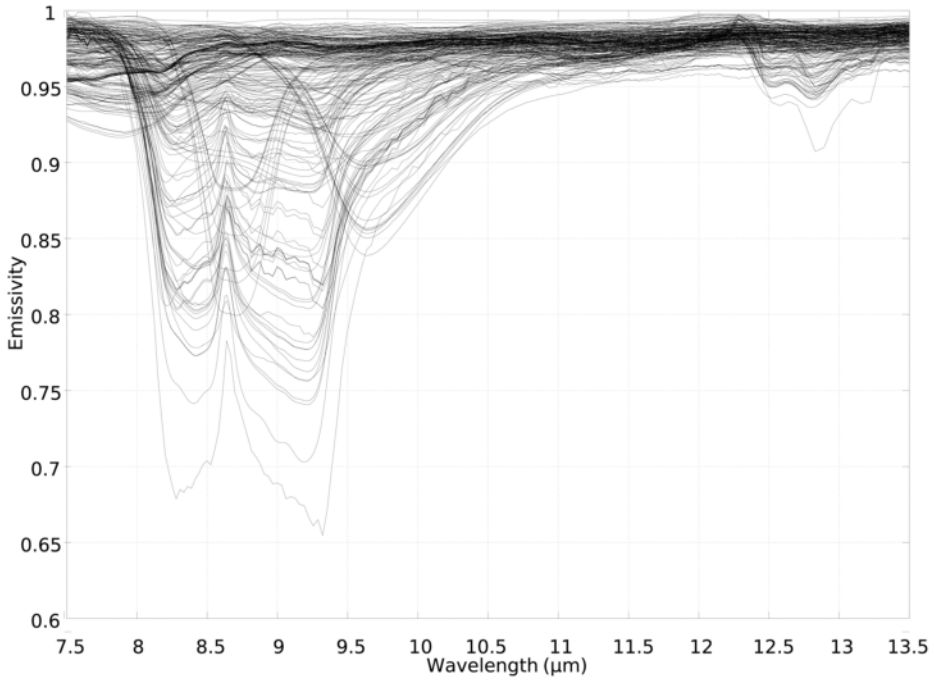


Fig. 2. 271 SAIL-generated emissivity spectra of vegetation canopy over soils.

architecture and vegetation/soil optical properties (LAI, ALA, spectra of leaf reflectance and transmittance, and spectra of soil reflectance), the dataset includes 63 700 spectra of emissivity of vegetated surface over the [7.5–13.5] $\mu$m spectral range.

Since large similarities appear between several simulated spectra of emissivity, and in order to reduce computation time, the database is reduced by selecting emissivity spectra using the Spectral Angle Mapper (SAM) method [88]. The resulting subset includes 271 emissivity spectra represented in Fig. 2. Eventually, and as described in § III-B, a random equal split of the dataset is conducted (Fig. 1). The first part, namely DB1, includes 135 spectra and is used for the simulations and for validation exercise. The second part, namely DB2, includes 136 spectra and is used to calibrate the MMD empirical relationship of the TES method.

We verify the robustness of the split between DB1 and DB2, by quantifying the variability of the calibrated coefficients for the TES empirical relationship when repeating the procedure 100 times on a random basis. The observed variability, about 1%–2% relative, confirms the robustness of the split.

### *B. Atmospheric Profile Dataset*

For documenting the atmospheric status, we used the MATISSE-v2 atmospheric profile database that includes three libraries called Air Force Geophysics Laboratory (AFGL)-lib, CLIMATO-lib, and Thermodynamic Initial Guess Retrieval (TIGR)3-lib.

1) AFGL-lib includes six profiles that are known as tropical, mid-latitude summer, mid-latitude winter, subarctic summer, subarctic winter, and 1976 US Standard [89].
2) CLIMATO-lib includes 144 profiles from a climatology database that provides an averaged thermodynamic profile for each latitude [90].
3) TIGR3-lib includes 2311 atmospheric profiles. It is a climatological library of representative atmospheric situations selected by statistical methods from 80 000 radiosonde-based profiles [91].

Each of the 2461 atmospheric profiles of the database includes vertical profiles of atmospheric pressure $P_{\text{atm}}(z)$, temperature $T_{\text{atm}}(z)$, humidity hr($z$), as well as of concentration in carbon dioxide [$CO_2$](z) and ozone [$O_3$](z).

Given the large size of the MATISSE-v2 atmospheric profile database, and in order to minimize the computation load, a first step consists of reducing the number of atmospheric profiles to construct a representative dataset without redundancy. This process is conducted by considering main drivers of atmospheric radiative transfer in the TIR domain, namely atmospheric water vapor content (AWVC), which drives atmospheric transmittance and emission, and equivalent atmospheric temperature $T_{\text{atm}}^{\text{eq}}$, which drives atmospheric emission. Both values are computed by following (22) and (23):

$$\text{AWVC} = \int_0^{z_{\max}} \rho_v(z)dz \tag{22}$$

$$T_{\text{eq}}^{\text{atm}} = \frac{\int_0^{z_{\max}} T_{\text{atm}}(z)\rho_v(z)dz}{\text{AWVC}} \tag{23}$$

where $z_{\max}$ is the highest altitude of the atmospheric profile and $\rho_v$ ($z$) is the water vapor density. Hence, the reduction method consists of selecting a set of profiles that verify two comparison criteria: 1) differences between two AWVC values are larger than 0.15 g.cm$^{-2}$ and 2) differences between two $T_{\text{eq}}^{\text{atm}}$ values are larger than 2 K. This reduction method leads to the selection of a subset of 248 atmospheric profiles among

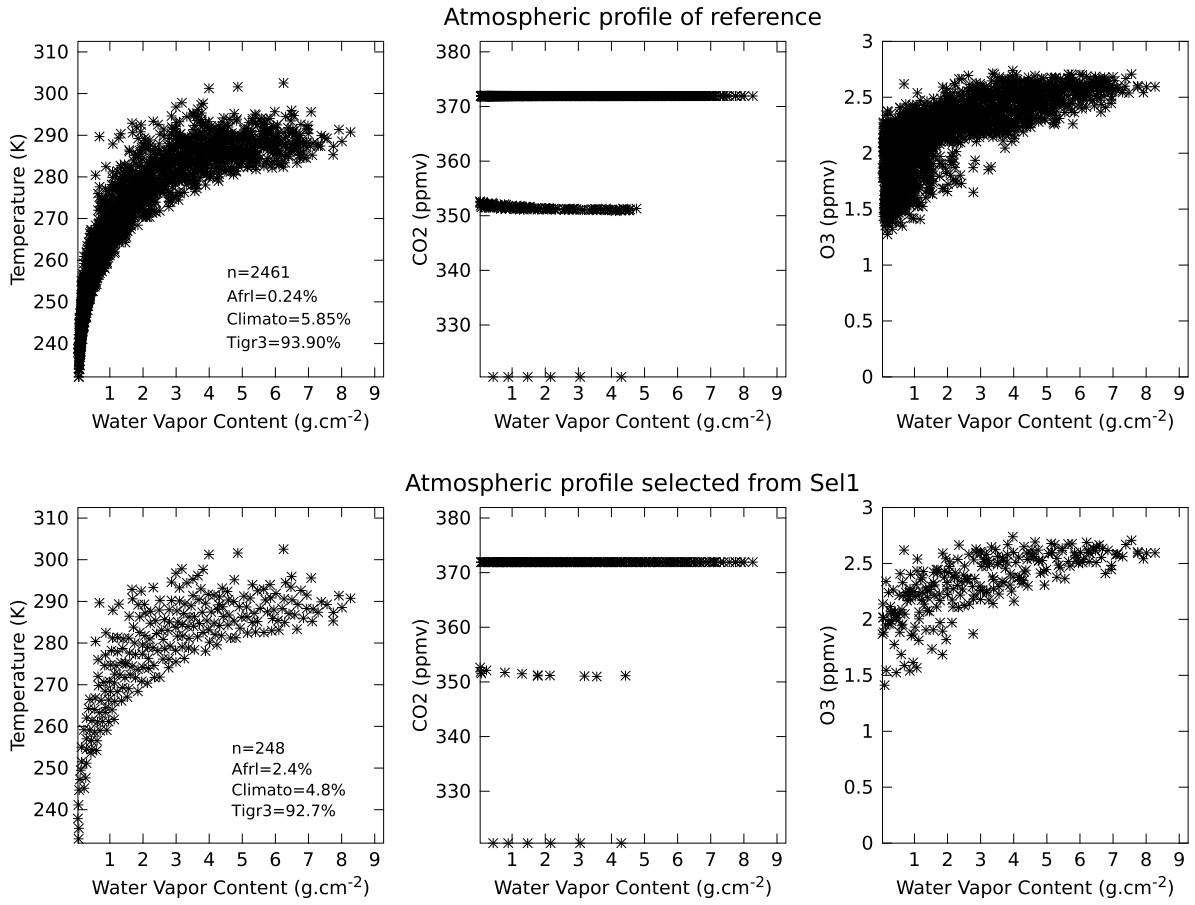


Fig. 3. Representation of the MATISSE-v2 and SEL1 subset of atmospheric profiles in the $\{T_{\text{atm}}^{\text{eq}}$, AWVC$\}$, $\{[CO_2]$, AWVC$\}$ and $\{[O_3]$, AWVC$\}$ spaces. AWVC and $T_{\text{atm}}^{\text{eq}}$ are computed using (22) and (23), respectively. $[CO_2]$ and $[O_3]$ are integrated values across the vertical profiles.

the 2461 initial profiles, hereafter referred to as SEL1 subset. Fig. 3 illustrates the distribution of the original dataset (top panels) and of the SEL1 subset (bottom panels) in the spaces $\{T_{\text{atm}}^{\text{eq}}$, AWVC$\}$, $\{[CO_2]$, AWVC$\}$, and $\{[O_3]$, AWVC$\}$. We note that the envelopes of the scatterplots are preserved, while their densities are reduced.

When conducting the inversion procedure to retrieve surface emissivity and radiometric temperature from the simulated MISTIGRI measurements (§ III-C), we account for uncertainties on atmospheric corrections by noising atmospheric profiles. When dealing with uncertainties on atmospheric temperature and humidity, we use the SEL1 subset of atmospheric profiles. For uncertainties on atmospheric concentrations of carbon dioxide $[CO_2]$ and ozone $[O_3]$, we use portions of the SEL1 subset, always with the objective of reducing the computation load. A portion of SEL1, namely SEL2, is generated by selecting SEL1 profiles that verify two comparison criteria: 1) differences between two AWVC values are larger than 1 g.cm$^{-2}$ and 2) differences between two vertically integrated values of $[CO_2(z)]$ are larger than 10 ppmv. Similarly, a portion of SEL1, namely SEL3, is generated by selecting SEL1 profiles that verify two comparison criteria: 1) differences between two AWVC values are larger than 0.5 g.cm$^{-2}$ and 2) differences between two vertically integrated values of $[0_3(z)]$ are larger than 0.15 ppmv. The resulting SEL2 and SEL3 selections contain 16 and 41 atmospheric profiles. We observe that SEL2 and SEL3 datasets are representative of the $[CO_2]$ and $[O_3]$ dynamics depicted by the SEL1 subset. Indeed, the envelopes of the scatterplots are preserved, while their densities are reduced (figure not shown).

### *C. Computation of Radiative Quantities and of Variables of Interest*

First, each of the 135 emissivity spectra of DB1 (see § IV-A) is associated with ten values of radiometric temperature $T_R^{\text{sur}}$. These temperatures are determined by a random selection within the [270–340] K interval, by setting up a constraint to provide realistic cases: for large canopy coverage (LAI larger than 4), the $T_R^{\text{sur}}$ value is lower than 315 K.

Second, each pair {emissivity spectra $\varepsilon_\lambda$, radiometric temperature $T_R^{\text{sur}}$} is combined with each atmospheric profile within the SEL1 subset, when the following condition is verified: $T_R^{\text{sur}} \in [T_{\text{atm}}$ (1)-10; $T_{\text{atm}}$ (1) + 30], where $T_{\text{atm}}$ (1) is the temperature of the lowest atmospheric level. For this, we combine each pair $\{\varepsilon_\lambda, T_R^{\text{sur}}\}$ with the triplet {atmospheric transmission $\tau_\lambda^{\text{atm}}$, atmospheric downwelling irradiance $E_\lambda^{\text{atm}\downarrow}$, atmospheric upwelling radiance $L_\lambda^{\text{atm}\uparrow}$} of any atmospheric profile, by using (10)–(12) to compute surface-leaving $L_\lambda^{\text{sur}\uparrow}$

and top-of-atmosphere $L_\lambda^{\mathrm{TOA}}$ radiances (Fig. 1). This process results in a number of simulated MISTIGRI measurements = 52 916 sets of $\mathrm{SBT}_j$, $\mathrm{TOABT}_j$ and of $\mathrm{OSBT}_j$ (Fig. 1).

Third, atmospheric profiles from subsets SEL1, SEL2 and SEL3 are noised on $T_{\mathrm{atm}}(z)$ and $\mathrm{hr}(z)$ only, on $[CO_2](z)$ only and on $[O_3](z)$ only, respectively, by following the procedure detailed in § III-C, to next calculate the corresponding radiative atmospheric quantities, namely $\tau_\lambda^{N\,\mathrm{atm}}$, $L_\lambda^{N\,\mathrm{atm}\uparrow}$ and $E_\lambda^{N\,\mathrm{atm}\downarrow}$. Then, the latter are used to perform atmospheric corrections in Module 4 (19) after convolution with channel filters [ISRF $S(\lambda)$, (15)]. Atmospheric corrections are performed on simulated data at the sensor level (prior to instrumental noise, $\mathrm{TOABT}_j$), and on simulated data of OS brightness temperature (after instrumental noises, $\mathrm{OSBT}_j$).

For both $\mathrm{OSBT}_j$ and $\mathrm{TOABT}_j$, atmospheric corrections using the SEL1, SEL2 and SEL3 subsets, respectively, result in $N_{\mathrm{ret}} = 52\,916$, 3126, and 8531 sets of corrected MISTIGRI measurements. Finally, the TES method is applied to all sets of atmospherically corrected MISTIGRI measurements. When dealing with $\mathrm{SBT}_j$, we apply TES on sensor measurements at the surface level by including errors on atmospheric downwelling radiance, which is consistent with former studies based on field measurements [71], [92]–[94].

## V. Setup of the SiMi Simulator for MISTIGRI

### A. Instrumental Configuration

As mentioned in the introduction, the solution chosen for the MISTIGRI was micro-bolometer sensors. This solution imposes to consider wide spectral channels of at least 0.5 $\mu$m FWHM, in order to minimize radiometric noise [NEDT, see (16)]. For comparison, in the case of the ASTER sensor, which used first-generation mercury–cadmium–telluride (MCT) detectors, the minimum FWHM is 0.25 $\mu$m [95]. The ISRF set for the reference configuration is provided by the sensor manufacturer (top panel of Fig. 4). This configuration includes four channels: TIR1 over [9.8–10.8] $\mu$m, TIR2 over [11–12] $\mu$m, TIR3 over [8.15–9.1] $\mu$m, and TIR4 over [8.6–9.55] $\mu$m. According to the sensor manufacturer, uncertainty on both central wavelengths $\lambda_j$ and FWHMs is 0.15 $\mu$m. For the current study, this reference configuration is disregarded since the TIR1 channel significantly overlaps the strong ozone absorption region around 9.6 $\mu$m.

From the reference configuration, other configurations are generated by varying the number of channels, their positions, and their FWHM, with the following constraints.

1) The number of spectral channels $N_b$ is fewer than five as regard to mission requirements, and greater than two in order to capture the spectral variability of natural surfaces, for the sake of consistency with the use of the TES method.
2) The spectral channels are as wide as possible to minimize instrumental noise, and as narrow as possible to capture emissivity variations, especially between 8 and 10 $\mu$m.
3) The spectral channels are located on atmospheric windows, i.e., spectral intervals where atmospheric transmittance is large.

From these considerations, six spectral configurations are proposed for the MISTIGRI mission (see Fig. 4): two sets of two configurations with $N_b = 4$ channels (MIS-1, MIS-2) on the one hand, and (MIS-3, MIS-4) on the other hand; as well as one set of two configurations with $N_b = 3$ channels (MIS-5, MIS-6). These six configurations are selected for the reasons discussed below.

1) The set of configurations (MIS-5, MIS-6) differs from the sets (MIS-1, MIS-2) and (MIS-3, MIS-4) by the number of spectral channels $N_b$. These differences permit to study the impact of channel number over the [8–10] $\mu$m spectral interval that is typified by large emissivity variations (see Fig. 2).
2) The sets (MIS-1, MIS-2) and (MIS-3, MIS-4) differ in the location of the two channels over the [8–10] $\mu$m range. Similarly, the MIS-5 and MIS-6 configurations differ in the location of the single channel over the [8–10] $\mu$m range. Again, these differences permit to study the impact of channel localization within the [8–10] $\mu$m spectral interval that is characterized by large emissivity variations (see Fig. 2).
3) The MIS-1 and MIS-2 configurations differ in channel widths for TIR1 and TIR2, as do MIS-3 and MIS-4 configurations for TIR3 and TIR4. These differences permit to evaluate the impact of channel FWHM.

Each spectral channel $j$ has a Gaussian shape with a central wavelength $\lambda_j$ and a $\mathrm{FWHM}_j$ (Table II).

From the abacuses provided by the manufacturer, the $\mathrm{NEDT}_j$ values are finally computed for all channels included in each of the six MISTIGRI spectral configurations to be evaluated (see Fig. 5). Any abacus expresses $\mathrm{NEDT}j$ as a function of both measured brightness temperature and channel width (FWHM). Using micro-bolometer detectors, $\mathrm{NEDT}_j$ is significantly larger when channel width decreases. Furthermore, $\mathrm{NEDT}_j$ decreases when the measured brightness temperature is larger, whereas channel central wavelength as a negligible impact.

### B. MMD Calibration and Validation

The empirical relationship $\varepsilon_{\min} = f(\mathrm{MMD})$ is calibrated by using the DB2 subset of emissivity spectra that contains 135 samples, and it is validated by using the 136 emissivity included into the DB1 subset. Emissivity spectra are ISRF-convolved by using the MISTIGRI spectral configurations defined in § V-A. Initial values of empirical coefficients are set according to previous studies [55]: $A = 0.994$, $B = -0.687$, and $C = 0.737$. Note that we obtained the same calibration results regardless of initial guess.

## VI. Results and Discussion

We report and discuss the results we obtain when calibrating the TES empirical relationship, and when validating the TES retrievals of emissivity and radiometric temperature. For TES retrievals, we report results by considering first uncertainties on atmospheric profiles of temperature and humidity, and second uncertainties on carbon dioxide and ozone concentrations. In both cases, we compare TES retrievals

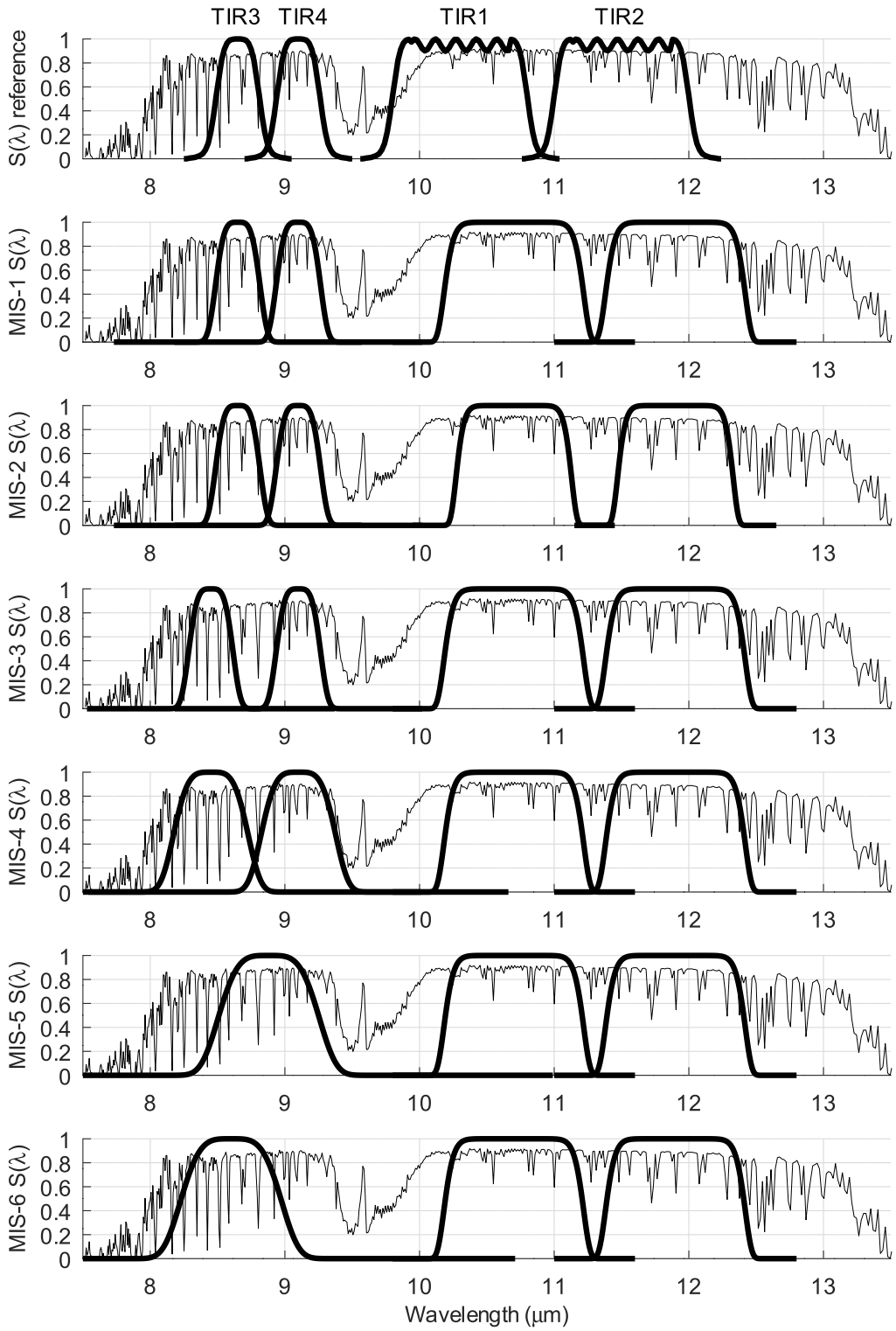


Fig. 4. Various MISTIGRI spectral configurations considered in the current study, typified by their ISRF, along with a typical example of atmospheric transmittance. Central wavelengths and FWHMs are given into Table II.

derived from brightness temperature at the surface level (TES-$\varepsilon_j^{\mathrm{BOA}}$, TES-$T_R^{\mathrm{sur,BOA}}$), from brightness temperature at the sensor level (TES-$\varepsilon_j^{\mathrm{TOA}}$, TES-$T_R^{\mathrm{sur,TOA}}$), and from out-of-sensor brightness temperature (TES-$\varepsilon_j^{\mathrm{OS}}$, TES-$T_R^{\mathrm{sur,OS}}$). The results are discussed in the light of spectral configuration, including channel number, widths, and locations, in order to highlight

TABLE II

SUMMARY OF THE SIX MISTIGRI SPECTRAL COMPOSITIONS WE CONSIDER IN THE CURRENT STUDY. CHANNELS ARE ORDERED ACCORDING TO INCREASING WAVELENGTHS

| Channel | TIR3 | | TIR4 | | TIR1 | | TIR2 | |
|---|---|---|---|---|---|---|---|---|
| | $\lambda_3$ | $\text{FWHM}_3$ | $\lambda_4$ | $\text{FWHM}_4$ | $\lambda_1$ | $\text{FWHM}_1$ | $\lambda_2$ | $\text{FWHM}_2$ |
| MIS-1 | 8.65 | 0.32 | 9.1 | 0.32 | 10.7 | 1.02 | 11.9 | 1.02 |
| MIS-2 | 8.65 | 0.32 | 9.1 | 0.32 | 10.7 | 0.84 | 11.9 | 0.84 |
| MIS-3 | 8.45 | 0.32 | 9.1 | 0.32 | 10.7 | 1.02 | 11.9 | 1.02 |
| MIS-4 | 8.45 | 0.54 | 9.1 | 0.54 | 10.7 | 1.02 | 11.9 | 1.02 |
| MIS-5 | 8.88 | 0.74 | - | - | 10.7 | 1.02 | 11.9 | 1.02 |
| MIS-6 | 8.60 | 0.74 | - | - | 10.7 | 1.02 | 11.9 | 1.02 |

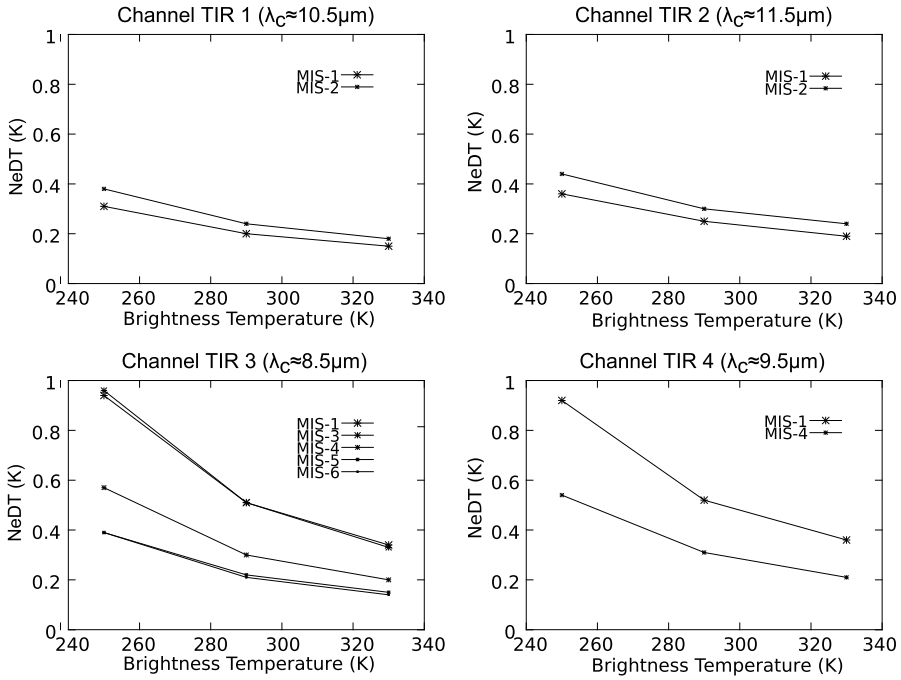


Fig. 5. NEDT values as a function of brightness temperature and channel width (FWHM), for all channels in each of the six MISTIGRI spectral configurations to be evaluated. A unique illustration is given when a channel is identical across several spectral configurations (see Table II for channel equality across configurations).

any influence of these factors in the context of the MISTIGRI mission.

### *A. Calibrating the TES Empirical Relationship*

Fig. 6 displays the MMD calibration results obtained for each of the six MISTIGRI configurations, along with the corresponding values for the *A*, *B*, and *C* coefficients (8) and the associated residual errors $\text{RMSE}_{\text{cal}}^{\varepsilon_{\min}}$ (17).

In all cases, the calibration results are good, with $\text{RMSE}_{\text{cal}}^{\varepsilon_{\min}}$ values lower than 0.007. The MIS-3 and MIS-4 configurations have the lowest calibration residual errors, which is ascribed to the combination of channel locations (subplots 4 and 5 in Fig. 4) and emissivity spectral dynamics (Fig. 2), where the location of TIR3 below 8.5 $\mu$m allows better capture of the spectral contrasts. The 3-channels configurations MIS-5 and MIS-6 have the largest calibration residual errors since they capture less spectral variability of emissivity with only one channel over the [8–9.5] $\mu$m spectral range. The *A*, *B*, and *C* coefficients are different from one configuration to another, but they are similar when channel numbers are equal, i.e., spectral configurations MIS-1 to MIS-4 with 4 channels versus spectral configurations MIS-5 and MIS-6 with 3 channels.

The validation results are very similar to the calibration results, both in error magnitude and error variations from one spectral configuration to another (figure not shown). Indeed, the $\text{RMSE}_{\text{val}}^{\varepsilon_{\min}}$ values are consistent with those obtained for calibration and remain as well below 0.007 for all MISTIGRI spectral configurations. However, the similitude between RMSE values for calibration and validation must be considered with caution. Indeed, the calibration and validation datasets are not fully independent since they are extracted from a unique dataset that was simulated by the same model. Overall, the calibration errors we report here are similar to those reported in previous studies [1], [56], [57], [62], [63], [66], [68], [74].

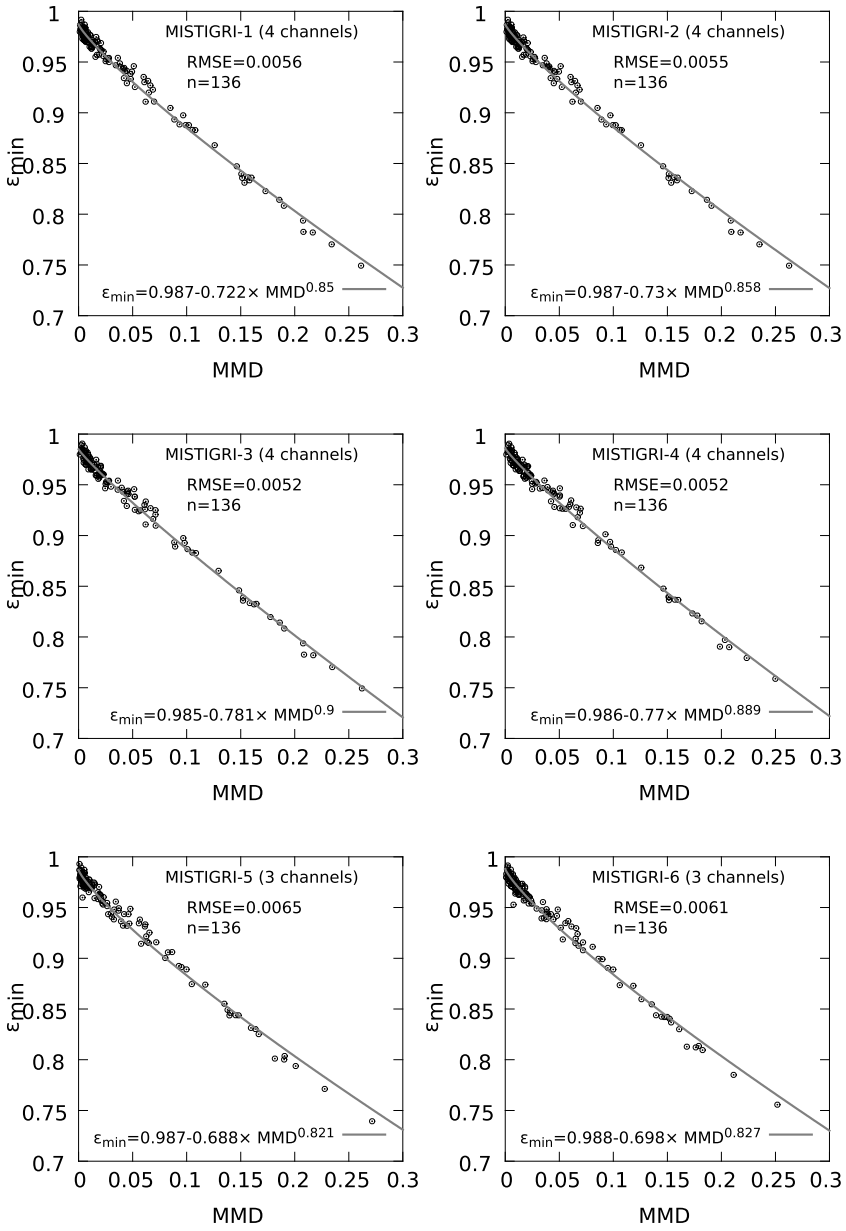


Fig. 6. Results of the $\varepsilon_{\min} = f(\text{MMD})$ calibration for each of the six MISTIGRI spectral configurations.

### *B. Retrieval Accuracies With Errors on Atmospheric Corrections Related to Temperature and Humidity*

Table III displays the validation results obtained with the TES method when using the SEL1 subset of atmospheric profiles noised on temperature and humidity. We consider each of the three types of retrievals to be considered (Fig. 1): retrievals from brightness temperatures $\text{SBT}_j$ at the surface level (TES-$\varepsilon_j^{\text{BOA}}$, TES-$T_R^{\text{sur,BOA}}$), retrievals from brightness temperatures $\text{TOABT}_j$ at the TOA (TES-$\varepsilon_j^{\text{TOA}}$, TES-$T_R^{\text{sur,TOA}}$), and retrievals from OS brightness temperature $\text{OSBT}_j$ at the TOA with instrumental noise (TES-$\varepsilon_j^{\text{OS}}$, TES-$T_R^{\text{sur,OS}}$).

For the BOA retrievals (TES-$\varepsilon_j^{\text{BOA}}$, TES-$T_R^{\text{sur,BOA}}$), the RMSE values on channel emissivities $\text{RMSE}_{\varepsilon_j^{\text{BOA}}}^{\text{TES}}$ and radiometric temperature $\text{RMSE}_{T_R^{\text{sur,BOA}}}^{\text{TES}}$ across all MISTIGRI configurations range between 0.005 and 0.009, and between 0.30 and 0.45 K, respectively. These RMSE values correspond to the errors due to the TES underlying assumptions (i.e., empirical relationship), as well as to the errors on the quantification of atmospheric downwelling radiance (§ IV-C). Regardless of spectral configuration, the relative variations in emissivity RMSE values across spectral channels range up to 20%, and larger RMSE values are observed at lower wavelengths. This can be explained by two factors in this range of wavelength. The first factor is related to sharp changes in emissivity between 8 and 9.5 $\mu$m, which are more difficult to capture as compared to flatter spectra portions between 10 and 12.5 $\mu$m (Fig. 2). The second factor is related to error propagation in the right term of (2), for which errors in emissivity combine with a magnitude

TABLE III

ERRORS ON RETRIEVALS OF EMISSIVITY AND RADIOMETRIC TEMPERATURE FROM THE TES METHOD ALONG WITH ATMOSPHERIC CORRECTIONS FROM PROFILES NOISED ON TEMPERATURE AND HUMIDITY. WE REPORT RMSE VALUES FOR 1) THE PAIR {TES-$\varepsilon_j^{\text{BOA}}$, TES-$T_R^{\text{sur,BOA}}$} THAT CORRESPONDS TO APPLYING THE TES METHOD ON SENSOR MEASUREMENTS OF SURFACE BRIGHTNESS TEMPERATURE AT THE SURFACE LEVEL, 2) FOR THE PAIR {TES-$\varepsilon_j^{\text{TOA}}$, TES-$T_R^{\text{sur,TOA}}$} THAT CORRESPONDS TO APPLYING ATMOSPHERIC CORRECTIONS AND THE TES METHOD ON TOA BRIGHTNESS TEMPERATURE AT THE SENSOR LEVEL, AND 3) THE PAIR {TES-$\varepsilon_j^{\text{OS}}$, TES-$T_R^{\text{sur,OS}}$} THAT CORRESPONDS TO APPLYING ATMOSPHERIC CORRECTIONS AND THE TES METHOD ON OS BRIGHTNESS TEMPERATURE (FIG. 1). CHANNEL EMISSIVITIES ARE ORDERED ACCORDING TO INCREASING WAVELENGTHS

| BOA | $\text{RMSE}_{\varepsilon_3^{BOA}}^{TES}$ | $\text{RMSE}_{\varepsilon_4^{BOA}}^{TES}$ | $\text{RMSE}_{\varepsilon_1^{BOA}}^{TES}$ | $\text{RMSE}_{\varepsilon_2^{BOA}}^{TES}$ | $\text{RMSE}_{T_R^{sur,BOA}}^{TES}$ |
|---|---|---|---|---|---|
| MIS-1 | 0.0077 | 0.0067 | 0.0061 | 0.0063 | 0.35 |
| MIS-2 | 0.0074 | 0.0065 | 0.0059 | 0.0061 | 0.34 |
| MIS-3 | 0.0071 | 0.0059 | 0.0054 | 0.0054 | 0.30 |
| MIS-4 | 0.0074 | 0.0059 | 0.0053 | 0.0054 | 0.30 |
| MIS-5 | 0.0084 | - | 0.0074 | 0.0077 | 0.43 |
| MIS-6 | 0.0086 | - | 0.0068 | 0.0070 | 0.40 |
| TOA | $RMSE_{\varepsilon_3^{TOA}}^{TES}$ | $RMSE_{\varepsilon_4^{TOA}}^{TES}$ | $RMSE_{\varepsilon_1^{TOA}}^{TES}$ | $RMSE_{\varepsilon_2^{TOA}}^{TES}$ | $RMSE_{T_R^{sur,TOA}}^{TES}$ |
| MIS-1 | 0.0112 | 0.0098 | 0.0082 | 0.0131 | 0.70 |
| MIS-2 | 0.0104 | 0.0093 | 0.0076 | 0.0141 | 0.68 |
| MIS-3 | 0.0124 | 0.0095 | 0.0076 | 0.0124 | 0.68 |
| MIS-4 | 0.0125 | 0.0100 | 0.0075 | 0.0121 | 0.69 |
| MIS-5 | 0.0118 | - | 0.0095 | 0.0135 | 0.78 |
| MIS-6 | 0.0122 | - | 0.0089 | 0.0128 | 0.76 |
| OS | $RMSE_{\varepsilon_3^{OS}}^{TES}$ | $RMSE_{\varepsilon_4^{OS}}^{TES}$ | $RMSE_{\varepsilon_1^{OS}}^{TES}$ | $RMSE_{\varepsilon_2^{OS}}^{TES}$ | $RMSE_{T_R^{sur,OS}}^{TES}$ |
| MIS-1 | 0.0299 | 0.0246 | 0.0203 | 0.0289 | 0.89 |
| MIS-2 | 0.0311 | 0.0251 | 0.0211 | 0.0321 | 0.91 |
| MIS-3 | 0.0376 | 0.0247 | 0.0203 | 0.0298 | 0.89 |
| MIS-4 | 0.0277 | 0.0194 | 0.0165 | 0.0258 | 0.79 |
| MIS-5 | 0.0191 | - | 0.0161 | 0.0232 | 0.85 |
| MIS-6 | 0.0212 | - | 0.0159 | 0.0230 | 0.83 |

of atmospheric downwelling irradiance that increases at lower wavelengths [57]. Given a large part of MMD values are below 0.03 over our dataset of simulated emissivity spectra (Fig. 6), this can also be explained by the gray body problem of the TES method that occurs over land surfaces with low spectral contrasts [36], [57], [70], [96]. When dealing with spectral configuration, the inclusion of one more channel over the [8–9.5] $\mu$m spectral interval induces slightly lower RMSE values on channel emissivities and radiometric temperature (i.e., MIS-1 to MIS-4 versus MIS-5 and MIS-6). This is associated with a better capture of spectral variability across the aforementioned spectral interval with large emissivity variations (Fig. 2). When considering the four-channels configurations, a larger gap between the TIR3 and TIR4 channels over the [8–9.5] $\mu$m spectral interval induces lower RMSE values (MIS-3 and MIS-4 versus MIS-1 and MIS-2), which is also explained by a better capture of spectral variability. Finally, decreasing channel widths over both spectral intervals (i.e., [8–9.5] $\mu$m and [10–12.5] $\mu$m) does not impact the captured spectral variability, since the RMSE values are similar (MIS-1 versus MIS-2 and MIS-3 versus MIS-4). Beyond the changes in RMSE values explained above, it is worth noting that differences in RMSE values remain low from one spectral configuration to another, up to 0.0023 and 0.13 K on channel emissivity and radiometric temperature, respectively.

For the TOA retrievals (TES-$\varepsilon_j^{\text{TOA}}$, TES-$T_R^{\text{sur,TOA}}$), the RMSE values on channel emissivities $RMSE_{\varepsilon_j^{\text{TOA}}}^{\text{TES}}$ and radiometric temperature $\text{RMSE}_{T_R^{\text{sur,TOA}}}^{\text{TES}}$ across all MISTIGRI configurations range between 0.008 and 0.0140, and between 0.70 and 0.80 K, respectively. These RMSE values are due to the combination of uncertainties related to the TES implementation (see the previous paragraph) and uncertainties on atmospheric corrections. Regardless of spectral configuration, the relative variations in emissivity RMSE values across spectral channels range up to 85%, and larger RMSE values are observed at extreme wavelengths, namely 8.6 and 11.9 $\mu$m. This is ascribed to lower atmospheric transmittances at these wavelengths (Fig. 4), which enhance errors on atmospheric corrections [36], [80], [97]. When dealing with spectral configuration, the inclusion of one more channel over the [8–9.5] $\mu$m spectral interval induces slightly lower RMSE values on channel emissivities and radiometric temperature (i.e., MIS-1 to MIS-4 versus MIS-5 and MIS-6), which, as in the BOA case, can be explained by a better capture of spectral variability. When considering the four-channels configurations, a larger gap between the TIR3 and TIR4 channels over the [8–9.5] $\mu$m spectral interval does not induce any change in RMSE values (MIS-3 and MIS-4 versus MIS-1 and MIS-2). This is converse to what is reported for the BOA retrievals, and it is therefore ascribed to uncertainties on atmospheric corrections. Finally, decreasing channel widths does not induce significant changes on RMSE values (MIS-1 versus MIS-2 and MIS-3 versus MIS-4). Overall, the differences in RMSE values remain low from one spectral configuration to another, up to 0.002 and

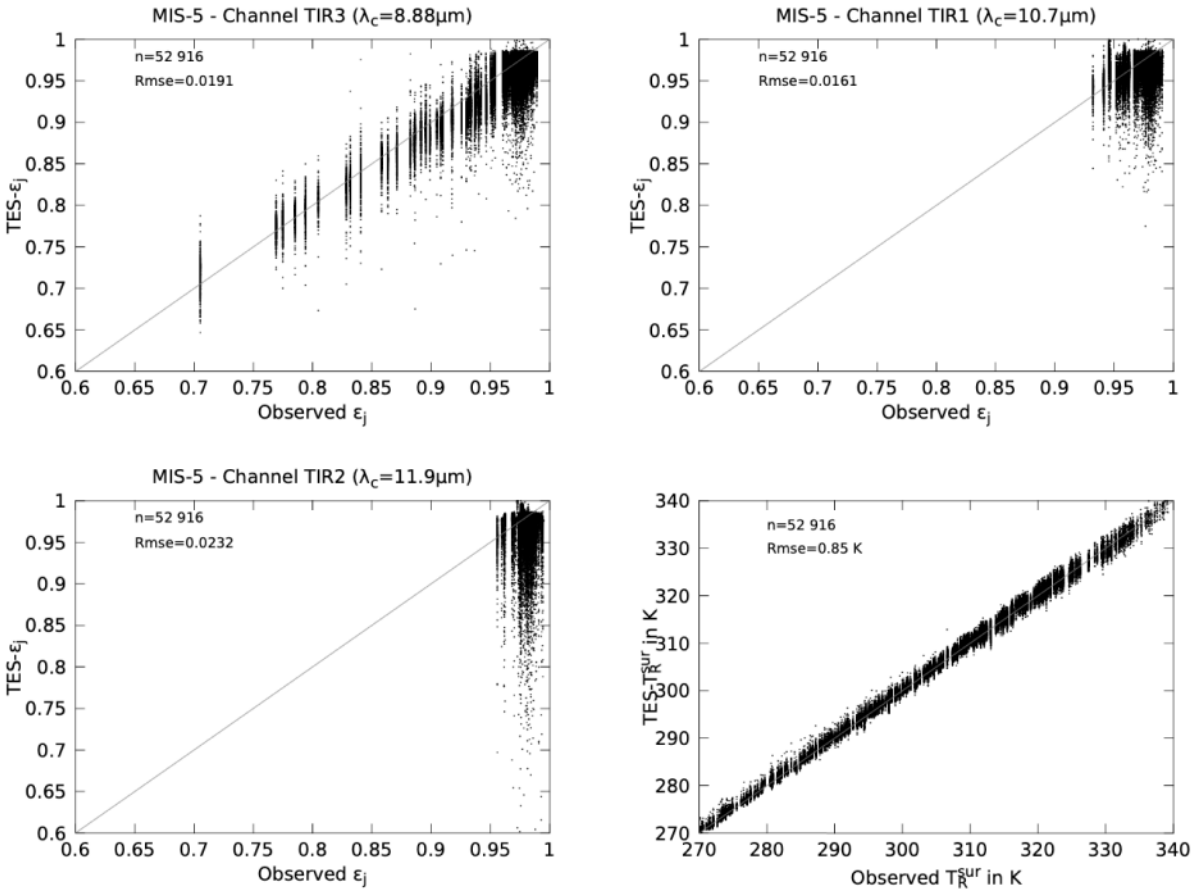


Fig. 7. Comparison of TES retrievals against reference values when considering 1) the MIS-5 spectral configuration with 3 channels (Fig. 4), 2) atmospheric corrections from atmospheric profiles noised on temperature and humidity, and 3) the TES retrievals of channel emissivities and radiometric temperature from OS brightness temperatures $\mathrm{OSBT}_j$ (TES-$\varepsilon_j^{\mathrm{OS}}$, TES-$T_R^{\mathrm{sur,OS}}$).

0.1 K on channel emissivity and radiometric temperature, respectively.

For the OS retrievals (TES-$\varepsilon_j^{\mathrm{OS}}$, TES-$T_R^{\mathrm{sur,OS}}$), the RMSE values on channel emissivities $\mathrm{RMSE}_{\varepsilon_j^{\mathrm{OS}}}^{\mathrm{TES}}$ and radiometric temperature $\mathrm{RMSE}_{T_R^{\mathrm{sur,OS}}}^{\mathrm{TES}}$ across all MISTIGRI configurations range between 0.0160 and 0.037, and between and 0.8 and 0.9 K, respectively. These larger RMSE values result from the combination of uncertainties related to the TES implementation, of uncertainties on atmospheric corrections, and of uncertainties induced by instrumental noise. Regardless of spectral configuration, the relative variations in emissivity RMSE values across spectral channels range up to 85%, and larger RMSE values are observed at extreme wavelengths, namely 8.6 and 11.9 $\mu$m. This is ascribed to the combined effects of uncertainties induced by instrumental noise and uncertainties on atmospheric corrections at wavelengths with lower atmospheric transmittances. Moreover, the RMSE values for emissivity are larger than in the TOA case, with increases up to a factor 3 for some channels, which highlights the impact of instrumental noise when dealing with micro-bolometer detectors. In terms of spectral configuration, the largest (respectively, lowest) RMSE values are observed for configurations with lowest (respectively, largest) channel widths, namely MIS-2 (respectively, MIS-5 and MIS-6), which is ascribed to the impact of channel width on instrumental noise (Fig. 5). Overall, the differences in RMSE values remain low from one spectral configuration to another, up to 0.0185 and 0.1 K on channel emissivity and radiometric temperature, respectively. Fig. 7 displays examples of scatterplots when considering the TES retrievals from OS brightness temperature $\mathrm{OSBT}_j$ after atmospheric corrections, for the three-channels spectral configuration MIS-5. It is shown that retrievals and reference values are in agreement for channel emissivity at 8.88 $\mu$m and radiometric temperature, whereas a moderate (respectively, large) discrepancy is observed for channel emissivity at 10.7 and 11.9 $\mu$m. Such discrepancies are not observed when validating TES retrievals from measurements of brightness temperature at the surface level [57], and they underline the impact of inaccurate atmospheric corrections on the performance of the TES method.

The aforementioned results for the BOA, TOA, and OS retrievals, permit to address the TES error budget at different levels and to compare the combined effects of uncertainties that accumulate at each step, namely TES implementation, atmospheric corrections, and instrumental noise related to the use of bolometer-based sensors.

1) First, the impacts of sharp emissivity changes at lower wavelengths (i.e., larger RMSE values for lower wavelengths, benefit of larger gap between channels within the [8–9.5] $\mu$m spectral interval, benefit of

TABLE IV

ERRORS ON RETRIEVALS OF EMISSIVITY AND RADIOMETRIC TEMPERATURE FROM THE TES METHOD ALONG WITH ATMOSPHERIC CORRECTIONS FROM PROFILES NOISED ON [$CO_2$]. WE REPORT RMSE VALUES FOR 1) THE PAIR {TES-$\varepsilon_j^{\mathrm{BOA}}$, TES-$T_R^{\mathrm{sur,BOA}}$} THAT CORRESPONDS TO APPLYING THE TES METHOD ON SENSOR MEASUREMENTS OF SURFACE BRIGHTNESS TEMPERATURE AT THE SURFACE LEVEL, 2) FOR THE PAIR {TES-$\varepsilon_j^{\mathrm{TOA}}$, TES-$T_R^{\mathrm{sur,TOA}}$} THAT CORRESPONDS TO APPLYING ATMOSPHERIC CORRECTIONS AND THE TES METHOD ON TOA BRIGHTNESS TEMPERATURE AT THE SENSOR LEVEL, AND 3) THE PAIR {TES-$\varepsilon_j^{\mathrm{OS}}$, TES-$T_R^{\mathrm{sur,OS}}$} THAT CORRESPONDS TO APPLYING ATMOSPHERIC CORRECTIONS AND THE TES METHOD ON OS BRIGHTNESS TEMPERATURE (FIG. 1). CHANNEL EMISSIVITIES ARE ORDERED ACCORDING TO INCREASING WAVELENGTHS

| BOA | $RMSE^{TES}_{\varepsilon_3^{BOA}}$ | $RMSE^{TES}_{\varepsilon_4^{BOA}}$ | $RMSE^{TES}_{\varepsilon_1^{BOA}}$ | $RMSE^{TES}_{\varepsilon_2^{BOA}}$ | $RMSE^{TES}_{T_R^{sur,BOA}}$ |
|---|---|---|---|---|---|
| MIS-1 | 0.0075 | 0.0066 | 0.0061 | 0.0063 | 0.34 |
| MIS-2 | 0.0073 | 0.0064 | 0.0058 | 0.0061 | 0.33 |
| MIS-3 | 0.007 | 0.0058 | 0.0054 | 0.0054 | 0.29 |
| MIS-4 | 0.0073 | 0.0058 | 0.0053 | 0.0054 | 0.29 |
| MIS-5 | 0.0082 | - | 0.0073 | 0.0076 | 0.41 |
| MIS-6 | 0.0085 | - | 0.0067 | 0.007 | 0.38 |
| TOA | $RMSE^{TES}_{\varepsilon_3^{TOA}}$ | $RMSE^{TES}_{\varepsilon_4^{TOA}}$ | $RMSE^{TES}_{\varepsilon_1^{TOA}}$ | $RMSE^{TES}_{\varepsilon_2^{TOA}}$ | $RMSE^{TES}_{T_R^{sur2}}$ |
| MIS-1 | 0.0102 | 0.008 | 0.0069 | 0.0061 | 0.35 |
| MIS-2 | 0.0086 | 0.0067 | 0.0058 | 0.0059 | 0.32 |
| MIS-3 | 0.0124 | 0.0077 | 0.0065 | 0.0055 | 0.32 |
| MIS-4 | 0.0129 | 0.0086 | 0.0065 | 0.0056 | 0.32 |
| MIS-5 | 0.0107 | - | 0.0084 | 0.0079 | 0.44 |
| MIS-6 | 0.0117 | - | 0.0078 | 0.0074 | 0.41 |
| OS | $RMSE^{TES}_{\varepsilon_3^{OS}}$ | $RMSE^{TES}_{\varepsilon_4^{OS}}$ | $RMSE^{TES}_{\varepsilon_1^{OS}}$ | $RMSE^{TES}_{\varepsilon_2^{OS}}$ | $RMSE^{TES}_{T_R^{sur,OS}}$ |
| MIS-1 | 0.0356 | 0.029 | 0.0249 | 0.0324 | 0.93 |
| MIS-2 | 0.0389 | 0.0324 | 0.0275 | 0.0385 | 0.99 |
| MIS-3 | 0.047 | 0.0305 | 0.0272 | 0.0383 | 0.97 |
| MIS-4 | 0.0336 | 0.0239 | 0.021 | 0.0332 | 0.76 |
| MIS-5 | 0.0245 | - | 0.0217 | 0.0249 | 0.8 |
| MIS-6 | 0.0276 | - | 0.0213 | 0.0269 | 0.79 |

a second channel over the [8–9.5] $\mu$m spectral interval) tend to vanish when accumulating errors induced by atmospheric corrections and uncertainties related to instrumental noise.

2) Second, the impact of errors on atmospheric correction is large, since it almost doubles the RMSE values on channel emissivities and radiometric temperature, with the largest impacts for channels located close to the atmospheric window boundaries (8 and 12.5 $\mu$m).
3) Third, consideration for additional instrumental noise significantly increases the errors on channel emissivity, but the resulting impact on radiometric temperature is limited. However, the benefit of adding a second channel over the [8–9.5] $\mu$m spectral interval is very limited when alternatively considering a unique channel with a large width. This underlines the balance between capturing spectral contrast and minimizing instrumental noise for bolometer-based sensors with large instrumental noise.

The MIS-5 configuration seems to be the most robust to the coupling of errors on atmospheric corrections and instrumental noise since it corresponds to the lowest error increase on radiometric temperature (from 0.43 to 0.85 K). In absolute terms, i.e., by adding the intrinsic uncertainty of TES, the most accurate configuration is MIS-4, since it provides the lowest error on radiometric temperature (0.79 K). Overall, the RMSE values that encompass all uncertainties range between 0.83 and 0.91 K across all MISTIGRI spectral configurations. This shows that the spectral configuration is not a critical issue for surface temperature retrieval in our study case with bolometer-based detectors. We note we deal here with accuracy on radiometric temperature, in accordance with the primary objectives of the MISTIGRI mission on land surface energy and water budgets. Nevertheless, we note that there is no systematic agreement between RMSE values on channel emissivities and on radiometric temperature, especially when the number of the channel varies (i.e., from three to four channels). This is ascribed to the high nonlinearity of the TES equation system (1)–(9), where any retrieval of radiometric temperature results from an iterative process that involves an incremental estimation of minimum emissivity across $N_b$ channels. Eventually, the TES performance we observe here is moderately larger than those reported in former studies also based on modeling approaches, with RMSE values ranging between 0.6 and 1 K [48], [59], [63], [74], [75].

### *C. Retrieval Accuracies With Errors on Atmospheric Corrections Related to Carbon Dioxide and Ozone Concentration*

Tables IV and V display the validation results obtained with the TES method when using the SEL2 and SEL3 subset of atmospheric profiles noised on [$CO_2$] and [$O_3$]. We consider each of the three types of retrievals to be considered (Fig. 1): retrievals from brightness temperatures $\mathrm{SBT}_j$ at the surface level (TES-$\varepsilon_j^{\mathrm{BOA}}$, TES-$T_R^{\mathrm{sur,BOA}}$), retrievals from brightness temperatures $\mathrm{TOABT}_j$ at the TOA (TES-$\varepsilon_j^{\mathrm{TOA}}$, TES-$T_R^{\mathrm{sur,TOA}}$), and retrievals from OS brightness temperature $\mathrm{OSBT}_j$ at the TOA with instrumental noise (TES-$\varepsilon_j^{\mathrm{OS}}$, TES-$T_R^{\mathrm{sur,OS}}$). Since the TES retrievals from brightness temperatures $\mathrm{SBT}_j$ at the surface level were previously analyzed in § VI-B, we do not discuss them here, and they are included in Tables IV and V to serve as references when analyzing 1) the TOA retrievals

TABLE V

ERRORS ON RETRIEVALS OF EMISSIVITY AND RADIOMETRIC TEMPERATURE FROM THE TES METHOD ALONG WITH ATMOSPHERIC CORRECTIONS FROM PROFILES NOISED ON [$O_3$]. WE REPORT RMSE VALUES FOR 1) THE PAIR {TES-$\varepsilon_j^{\mathrm{BOA}}$, TES-$T_R^{\mathrm{sur,BOA}}$} THAT CORRESPONDS TO APPLYING THE TES METHOD ON SENSOR MEASUREMENTS OF SURFACE BRIGHTNESS TEMPERATURE AT THE SURFACE LEVEL, 2) FOR THE PAIR {TES-$\varepsilon_j^{\mathrm{TOA}}$, TES-$T_R^{\mathrm{sur,TOA}}$} THAT CORRESPONDS TO APPLYING ATMOSPHERIC CORRECTIONS AND THE TES METHOD ON TOA BRIGHTNESS TEMPERATURE AT THE SENSOR LEVEL, AND 3) THE PAIR {TES-$\varepsilon_j^{\mathrm{OS}}$, TES-$T_R^{\mathrm{sur,OS}}$} THAT CORRESPONDS TO APPLYING ATMOSPHERIC CORRECTIONS AND THE TES METHOD ON OS BRIGHTNESS TEMPERATURE (FIG. 1). CHANNEL EMISSIVITIES ARE ORDERED ACCORDING TO INCREASING WAVELENGTHS

| BOA | $RMSE^{TES}_{\varepsilon_3^{BOA}}$ | $RMSE^{TES}_{\varepsilon_4^{BOA}}$ | $RMSE^{TES}_{\varepsilon_1^{BOA}}$ | $RMSE^{TES}_{\varepsilon_2^{BOA}}$ | $RMSE^{TES}_{T_R^{sur1}}$ |
|---|---|---|---|---|---|
| MIS-1 | 0.0075 | 0.0067 | 0.0061 | 0.0063 | 0.35 |
| MIS-2 | 0.0073 | 0.0065 | 0.0059 | 0.0061 | 0.34 |
| MIS-3 | 0.007 | 0.0058 | 0.0054 | 0.0054 | 0.3 |
| MIS-4 | 0.0073 | 0.0059 | 0.0053 | 0.0054 | 0.3 |
| MIS-5 | 0.0083 | - | 0.0074 | 0.0076 | 0.42 |
| MIS-6 | 0.0085 | - | 0.0068 | 0.007 | 0.39 |
| TOA | $RMSE^{TES}_{\varepsilon_3^{TOA}}$ | $RMSE^{TES}_{\varepsilon_4^{TOA}}$ | $RMSE^{TES}_{\varepsilon_1^{TOA}}$ | $RMSE^{TES}_{\varepsilon_2^{TOA}}$ | $RMSE^{TES}_{T_R^{sur,TOA}}$ |
| MIS-1 | 0.0102 | 0.0081 | 0.0068 | 0.0062 | 0.36 |
| MIS-2 | 0.0087 | 0.0069 | 0.0059 | 0.0059 | 0.33 |
| MIS-3 | 0.0118 | 0.0078 | 0.0064 | 0.0055 | 0.32 |
| MIS-4 | 0.012 | 0.009 | 0.0064 | 0.0056 | 0.33 |
| MIS-5 | 0.0109 | - | 0.0084 | 0.0079 | 0.45 |
| MIS-6 | 0.0113 | - | 0.0077 | 0.0073 | 0.42 |
| OS | $RMSE^{TES}_{\varepsilon_3^{OS}}$ | $RMSE^{TES}_{\varepsilon_4^{OS}}$ | $RMSE^{TES}_{\varepsilon_1^{OS}}$ | $RMSE^{TES}_{\varepsilon_2^{OS}}$ | $RMSE^{TES}_{T_R^{sur,OS}}$ |
| MIS-1 | 0.0367 | 0.0304 | 0.025 | 0.0303 | 0.89 |
| MIS-2 | 0.0384 | 0.0312 | 0.0267 | 0.0386 | 0.94 |
| MIS-3 | 0.05 | 0.0332 | 0.0413 | 0.0592 | 0.9 |
| MIS-4 | 0.0378 | 0.026 | 0.0229 | 0.0307 | 0.79 |
| MIS-5 | 0.0243 | - | 0.0206 | 0.0262 | 0.79 |
| MIS-6 | 0.0288 | - | 0.0217 | 0.0255 | 0.79 |

that involve errors on atmospheric corrections related to [$CO_2$] and [$O_3$], and 2) the OS retrievals that additionally involve uncertainties related to instrumental noise. We note the results for BOA retrievals are not identical in Tables III–V, since they correspond to different numbers of retrievals (52 916 with the SEL1 subset, 3126 with the SEL2 subset, and 8531 with the SEL3 subset, see § IV-C), as well as to different values for noised atmospheric downwelling irradiance.

For the TOA retrievals (TES-$\varepsilon_j^{\mathrm{TOA}}$, TES-$T_R^{\mathrm{sur,TOA}}$), the RMSE values on channel emissivities $\mathrm{RMSE}^{\mathrm{TES}}_{\varepsilon_j^{\mathrm{TOA}}}$ and radiometric temperature $\mathrm{RMSE}^{\mathrm{TES}}_{T_R^{\mathrm{sur,TOA}}}$ across all MISTIGRI configurations range between 0.060 and 0.013, and between 0.30 and 0.45 K, respectively, for both SEL2 and SEL3 subsets of atmospheric profiles noised on [$CO_2$] and [$O_3$]. Across both subsets, errors on TOA retrievals are very similar to those observed on BOA retrievals, which indicates that errors on atmospheric corrections related to [$CO_2$] and [$0_3$] have a very small impact on the TES retrievals.

For the OS retrievals (TES-$\varepsilon_j^{\mathrm{OS}}$, TES-$T_R^{\mathrm{sur,OS}}$), the RMSE values on channel emissivities $\mathrm{RMSE}^{\mathrm{TES}}_{\varepsilon_j^{\mathrm{OS}}}$ and radiometric temperature $\mathrm{RMSE}^{\mathrm{TES}}_{T_R^{\mathrm{sur,OS}}}$ across all MISTIGRI configurations range between 0.02 and 0.05, and between 0.8 and 1 K, respectively, for both SEL2 and SEL3 subsets. Thus, additional consideration of instrumental noise has a significant impact on the RMSE values, since these values reach the same magnitude than those reported for TOA retrievals with the SEL1 subset (Table III). This indicates that the impact on TES retrievals of uncertainties due to instrumental noise is similar to that of errors on atmospheric corrections related to atmospheric temperature and humidity. Then, the similar RMSE values observed for TOA and OS retrievals in Table III are explained by compensation effects between atmospheric and instrumental perturbations, the latter being characterized by Gaussian processes (13) and (14).

Eventually, and similar to the result obtained with the SEL1 subset, the spectral configuration that seems robust to coupling between [$CO_2$]/[$O_3$] concentration errors and instrumental noise is MIS-5. In absolute terms, the most accurate configuration is still MIS-4, although the differences with the other configurations also remain small (Tables IV and V).

### *D. Sensitivity of the MISTIGRI/TES Retrievals to Uncertainties on Channel Location and Bandwidths*

Our results also provide information about the sensitivity of the TES retrievals to uncertainties on MISTIGRI channel locations and widths, which is an important issue for sensor design and subsequent accuracy on emissivity/temperature retrievals. On the one hand, uncertainty on both channel locations and widths is 0.15 $\mu$m, according to the information provided by the detector manufacturer (§ V-A). On the other hand, the variability on channel location and widths across the six MISTIGRI spectral configurations is slightly larger than the aforementioned uncertainty, i.e., around 0.2 $\mu$m, as indicated in Fig. 4 and Table II. Therefore, it is possible to evaluate the impact of this uncertainty, by quantifying the variability we observe on TES retrieval accuracy across the six MISTIGRI spectral configurations.

On the basis of the TES retrieval accuracy across the six configurations, for each of the three cases (BOA, TOA, OS) reported by Tables III–V, we note a variability on TES retrieval accuracy that ranges between 0.05 and 0.15 K. This underlines

the low impact of changes in channel locations and bandwidths, and therefore the low impact of uncertainty on channel locations and bandwidths. Eventually, we note that changes between the six spectral configurations (i.e., channel locations and bandwidth) are similar to the uncertainty on channel locations and bandwidths. Indeed, the variability across spectral configurations is constrained by both channel overlaps and atmospheric windows, notably because of large bandwidths. This highlights that using bolometer-based detectors induces a tradeoff between instrumental noise and bandwidth. Such a constraint should be overcome by using the last generation of MCT cooled detectors.

## VII. Concluding Remarks

The current study aims to propose an appropriate spectral configuration for the micro-bolometer-based TIR sensor of the MISTIGRI mission.

The strategy is typified by the following points. First, we address the various errors related to each step of the retrieval procedure: the TES underlying assumptions about emissivity spectral contrast, the errors on atmospheric corrections related to knowledge about atmospheric status when the satellite overpasses, and the instrumental noise related to filter response functions for micro-bolometer-based detectors. Second, when dealing with uncertainties on atmospheric status, we consider atmospheric profiles of temperature and humidity, as well as of carbon dioxide and ozone concentrations. Third, the error budget analysis is based on numerical model simulations, by including the last generation of land surface emissivity spectra that account for the cavity effect. Fourth, we evaluate six predefined spectral configurations for the MISTIGRI TIR sensor, where the spectral configurations differ in terms of channel number, locations, and widths.

On the basis of the error budget analysis, the main outcomes of the current study are the following. First, errors on atmospheric corrections related to knowledge on temperature and humidity profiles have a similar impact on TES retrievals than uncertainties related to instrumental noise. The equivalence in contribution to the error budget is ascribed to the large instrumental errors due to the use of micro-bolometer detectors. The resulting errors on TES retrievals are twice as large as those due to the TES underlying assumption about emissivity spectral contrast. Second, retrieval accuracies are very similar across all MISTIGRI spectral configurations, where differences are within 0.2 K on radiometric temperature. This shows that the spectral configuration to be chosen is not a critical issue in our study case that addresses the use of micro-bolometer-based sensing with significant instrumental noises or large channel widths. Third, retrieval accuracies on radiometric temperature are moderately larger than those reported in former studies based on numerical model simulations, for MCT cooled detectors such as ASTER or ECOSTRESS sensors.

The main limitations of the current study, to be overcome with on-going works, are the following. First, we consider a micro-bolometer-based sensor, and results may vary if considering the last generation of MCT cooled detectors that permit to reduce both channel widths and instrumental noises. In this case, the challenge is to increase the accuracy of atmospheric corrections. Second, we consider a set of predefined spectral configurations to be evaluated by analyzing the simulation-based error budget. However, results are expected to be more robust if using an optimization procedure that combines the simultaneous sliding of several channels, since it is possible to identify a global minimum on retrieval errors.

From a practical point of view, eventually, the study succeeds in defining the most suited spectral configuration for the MISTIGRI sensor, i.e., the spectral configuration that provides retrievals of land surface radiometric temperature with lower errors.

## References

[1] G. C. Hulley and S. J. Hook, "Generating consistent land surface temperature and emissivity products between ASTER and MODIS data for Earth science research," *IEEE Trans. Geosci. Remote Sens.*, vol. 49, no. 4, pp. 1304–1315, Apr. 2011.

[2] K. Ogawa, T. Schmugge, F. Jacob, and A. French, "Estimation of broadband land surface emissivity from multi-spectral thermal infrared remote sensing," *Agronomie*, vol. 22, no. 6, pp. 695–696, 2002.

[3] K. Ogawa, T. Schmugge, F. Jacob, and A. French, "Estimation of land surface window (8–12 $\mu$m) emissivity from multi-spectral thermal infrared remote sensing—A case study in a part of Sahara desert," *Geophys. Res. Lett.*, vol. 30, no. 2, pp. 1–4, Jan. 2003.

[4] M. Mira *et al.*, "Uncertainty assessment of surface net radiation derived from Landsat images," *Remote Sens. Environ.*, vol. 175, pp. 251–270, Mar. 2016.

[5] G. Yan, Z.-H. Jiao, T. Wang, and X. Mu, "Modeling surface longwave radiation over high-relief terrain," *Remote Sens. Environ.*, vol. 237, Feb. 2020, Art. no. 111556.

[6] G. Bigeard *et al.*, "Ability of a soil–vegetation–atmosphere transfer model and a two-source energy balance model to predict evapotranspiration for several crops and climate conditions," *Hydrol. Earth Syst. Sci.*, vol. 23, no. 12, pp. 5033–5058, Dec. 2019.

[7] A. French *et al.*, "Surface energy fluxes with the advanced spaceborne thermal emission and reflection radiometer (ASTER) at the Iowa 2002 SMACEX site (USA)," *Remote Sens. Environ.*, vol. 99, pp. 55–65, Nov. 2005.

[8] M. Galleguillos, F. Jacob, L. Prévot, P. Lagacherie, and L. Shunlin, "Mapping daily evapotranspiration over a Mediterranean vineyard watershed," *IEEE Geosci. Remote Sens. Lett.*, vol. 8, no. 1, pp. 168–172, Jan. 2011.

[9] M. Gokmen, Z. Vekerdy, A. Verhoef, W. Verhoef, O. Batelaan, and C. van der Tol, "Integration of soil moisture in SEBS for improving evapotranspiration estimation under water stress conditions," *Remote Sens. Environ.*, vol. 121, pp. 261–274, Jun. 2012.

[10] M. Gómez, A. Olioso, J. A. Sobrino, and F. Jacob, "Retrieval of evapotranspiration over the Alpilles/ReSeDA experimental site using airborne POLDER sensor and a thermal camera," *Remote Sens. Environ.*, vol. 96, pp. 399–408, Jun. 2005.

[11] F. Jacob, A. Olioso, X. F. Gu, Z. Su, and B. Seguin, "Mapping surface fluxes using airborne visible, near infrared, thermal infrared remote sensing data and a spatialized surface energy balance model," *Agronomie*, vol. 22, no. 6, pp. 669–680, 2002.

[12] C. Montes, J.-P. Lhomme, J. Demarty, L. Prévot, and F. Jacob, "A three-source SVAT modeling of evaporation: Application to the seasonal dynamics of a grassed vineyard," *Agricult. Forest Meteorol.*, vol. 191, pp. 64–80, Jun. 2014.

[13] C. Montes and F. Jacob, "Comparing Landsat-7 ETM+ and ASTER imageries to estimate daily evapotranspiration within a Mediterranean vineyard watershed," *IEEE Geosci. Remote Sens. Lett.*, vol. 14, no. 3, pp. 459–463, Mar. 2017.

[14] N. Pardo, M. L. Sánchez, J. Timmermans, Z. Su, I. A. Pérez, and M. A. García, "SEBS validation in a Spanish rotating crop," *Agricult. Forest Meteorol.*, vols. 195–196, pp. 132–142, Sep. 2014.

[15] R. K. Vinukollu, E. F. Wood, C. R. Ferguson, and J. B. Fisher, "Global estimates of evapotranspiration for climate studies using multi-sensor remote sensing data: Evaluation of three process-based approaches," *Remote Sens. Environ.*, vol. 115, no. 3, pp. 801–823, Mar. 2011.

[16] T. N. Carlson and G. P. Petropoulos, "A new method for estimating of evapotranspiration and surface soil moisture from optical and thermal infrared measurements: The simplified triangle," *Int. J. Remote Sens.*, vol. 40, no. 20, pp. 7716–7729, Oct. 2019.

[17] J. A. Sobrino, B. Franch, C. Mattar, J. C. Jiménez-Muñoz, and C. Corbari, "A method to estimate soil moisture from airborne hyperspectral scanner (AHS) and ASTER data: Application to SEN2FLEX and SEN3EXP campaigns," *Remote Sens. Environ.*, vol. 117, pp. 415–428, Feb. 2012.

[18] J. A. Taylor, F. Jacob, M. Galleguillos, L. Prévot, N. Guix, and P. Lagacherie, "The utility of remotely-sensed vegetative and terrain covariates at different spatial resolutions in modelling soil and watertable depth (for digital soil mapping)," *Geoderma*, vols. 193–194, pp. 83–93, Feb. 2013.

[19] D. Courault *et al.*, "Influence of agricultural practices on micrometeorological spatial variations at local and regional scales," *Int. J. Remote Sens.*, vol. 30, no. 5, pp. 1183–1205, Mar. 2009.

[20] B. Cao *et al.*, "A review of Earth surface thermal radiation directionality observing and modeling: Historical development, current status and perspectives," *Remote Sens. Environ.*, vol. 232, Oct. 2019, Art. no. 111304.

[21] J.-P. Lagouarde *et al.*, "Modelling daytime thermal infrared directional anisotropy over Toulouse city centre," *Remote Sens. Environ.*, vol. 114, no. 1, pp. 87–105, Jan. 2010.

[22] J. P. Lagouarde *et al.*, "Experimental characterization and modelling of the nighttime directional anisotropy of thermal infrared measurements over an urban area: Case study of Toulouse (France)," *Remote Sens. Environ.*, vol. 117, pp. 19–33, Feb. 2012.

[23] I. M. Watson *et al.*, "Thermal infrared remote sensing of volcanic emissions using the moderate resolution imaging spectroradiometer," *J. Volcanol. Geothermal Res.*, vol. 135, nos. 1–2, pp. 75–89, Jul. 2004.

[24] P. Lundgren *et al.*, "The dynamics of large silicic systems from satellite remote sensing observations: The intriguing case of Domuyo volcano, Argentina," *Sci. Rep.*, vol. 10, no. 1, pp. 1–15, Dec. 2020.

[25] G. Ganci *et al.*, "A year of lava fountaining at Etna: Volumes from SEVIRI," *Geophys. Res. Lett.*, vol. 39, no. 6, pp. 1–6, Mar. 2012.

[26] H.-P. Chan, C.-P. Chang, T.-H. Lin, M. Blackett, H. Kuo-Chen, and A. T.-S. Lin, "The potential of satellite remote sensing for monitoring the onset of volcanic activity on Taipei's doorstep," *Int. J. Remote Sens.*, vol. 41, no. 4, pp. 1372–1388, Feb. 2020.

[27] F. van der Meer, C. Hecker, F. van Ruitenbeek, H. van der Werff, C. de Wijkerslooth, and C. Wechsler, "Geologic remote sensing for geothermal exploration: A review," *Int. J. Appl. Earth Observ. Geoinf.*, vol. 33, pp. 255–269, Dec. 2014.

[28] Y. Ninomiya and B. Fu, "Thermal infrared multispectral remote sensing of lithology and mineralogy based on spectral properties of materials," *Ore Geol. Rev.*, vol. 108, pp. 54–72, May 2019.

[29] N. Karimi, A. Farokhnia, L. Karimi, M. Eftekhari, and H. Ghalkhani, "Combining optical and thermal remote sensing data for mapping debris-covered glaciers (Alamkouh Glaciers, Iran)," *Cold Regions Sci. Technol.*, vol. 71, pp. 73–83, Feb. 2012.

[30] V. Singh and M. K. Goyal, "An improved coupled framework for glacier classification: An integration of optical and thermal infrared remote-sensing bands," *Int. J. Remote Sens.*, vol. 39, no. 20, pp. 6864–6892, Oct. 2018.

[31] C. J. Donlon, M. Martin, J. Stark, J. Roberts-Jones, E. Fiedler, and W. Wimmer, "The operational sea surface temperature and sea ice analysis (OSTIA) system," *Remote Sens. Environ.*, vol. 116, pp. 140–158, Jan. 2012.

[32] T. Kuleli and S. Bayazit, "Summer season sea surface temperature changes in the Aegean Sea based on 30 years (1989–2019) of Landsat thermal infrared data," *Environ. Monitor. Assessment*, vol. 192, no. 11, pp. 1–13, Nov. 2020.

[33] J. R. Irons, J. L. Dwyer, and J. A. Barsi, "The next Landsat satellite: The Landsat data continuity mission," *Remote Sens. Environ.*, vol. 122, pp. 11–21, Jul. 2012.

[34] D. P. Roy *et al.*, "Landsat-8: Science and product vision for terrestrial global change research," *Remote Sens. Environ.*, vol. 145, pp. 154–172, Apr. 2014.

[35] A. Gillespie *et al.*, "A temperature and emissivity separation algorithm for advanced spaceborne thermal emission and reflection radiometer (ASTER) images," *IEEE Trans. Geosci. Remote Sens.*, vol. 36, no. 4, pp. 1113–1126, Apr. 1998.

[36] F. Jacob, F. Petitcolin, T. Schmugge, É. Vermote, A. French, and K. Ogawa, "Comparison of land surface emissivity and radiometric temperature derived from MODIS and ASTER sensors," *Remote Sens. Environ.*, vol. 90, no. 2, pp. 137–152, Mar. 2004.

[37] A. P. Cracknell, *Advanced Very High Resolution Radiometer AVHRR*. Boca Raton, FL, USA: CRC Press, 1997.

[38] Z. Song, S. Liang, D. Wang, Y. Zhou, and A. Jia, "Long-term record of top-of-atmosphere albedo over land generated from AVHRR data," *Remote Sens. Environ.*, vol. 211, pp. 71–88, Jun. 2018.

[39] D. M. A. Aminou, B. Jacquet, and F. Pasternak, "Characteristics of the meteosat second generation (MSG) radiometer/imager: Seviri," *Proc. SPIE*, vol. 3221, pp. 19–31, Dec. 1997.

[40] I. F. Trigo *et al.*, "The satellite application facility for land surface analysis," *Int. J. Remote Sens.*, vol. 32, no. 10, pp. 2725–2744, May 2011.

[41] A. Savtchenko, D. Ouzounov, A. Gopalan, D. Yuan, D. Nickless, and D. Ostrenga, "MODIS data from Terra and Aqua satellites," in *Proc. IEEE Int. Geosci. Remote Sens. Symp. (IGARSS)*, vol. 5, Jul. 2003, pp. 3028–3030.

[42] V. V. Salomonson, W. Barnes, and E. J. Masuoka, "Introduction to MODIS and an overview of associated activities," in *Earth Science Satellite Remote Sensing*. Berlin, Germany: Springer, 2006, pp. 12–32.

[43] D. Smith *et al.*, "Sentinel-3A/B SLSTR pre-launch calibration of the thermal InfraRed channels," *Remote Sens.*, vol. 12, no. 16, p. 2510, Aug. 2020.

[44] O. Merlin *et al.*, "Disaggregation of MODIS surface temperature over an agricultural area using a time series of Formosat-2 images," *Remote Sens. Environ.*, vol. 114, no. 11, pp. 2500–2512, Nov. 2010.

[45] O. Merlin, F. Jacob, J.-P. Wigneron, J. Walker, and G. Chehbouni, "Multidimensional disaggregation of land surface temperature using high-resolution red, near-infrared, shortwave-infrared, and microwave-L bands," *IEEE Trans. Geosci. Remote Sens.*, vol. 50, no. 5, pp. 1864–1880, May 2012.

[46] B. Seguin *et al.*, "IRSUTE: A minisatellite project for land surface heat flux estimation from field to regional scale," *Remote Sens. Environ.*, vol. 68, no. 3, pp. 357–369, 1999.

[47] J. A. Sobrino and J. C. Jiménez-Muñoz, "Land surface temperature retrieval from thermal infrared data: An assessment in the context of the surface processes and ecosystem changes through response analysis (SPECTRA) mission," *J. Geophys. Res., Atmos.*, vol. 110, no. D16, pp. 1–10, 2005.

[48] G. Hulley, S. Hook, J. Fisher, and C. Lee, "ECOSTRESS, a NASA Earth-ventures instrument for studying links between the water cycle and plant health over the diurnal cycle," in *Proc. IEEE Int. Geosci. Remote Sens. Symp. (IGARSS)*, Jul. 2017, pp. 5494–5496.

[49] B. Koetz *et al.*, "High spatio-temporal resolution land surface temperature mission—A Copernicus candidate mission in support of agricultural monitoring," in *Proc. IEEE Int. Geosci. Remote Sens. Symp. (IGARSS)*, Jul. 2018, pp. 8160–8162.

[50] J.-P. Lagouarde *et al.*, "The MISTIGRI thermal infrared project: Scientific objectives and mission specifications," *Int. J. Remote Sens.*, vol. 34, nos. 9–10, pp. 3437–3466, 2013.

[51] J.-P. Lagouarde *et al.*, "Indo-French high-resolution thermal infrared space mission for Earth natural resources assessment and monitoring-concept and definition of TRISHNA," in *Proc. ISPRS-GEOGLAM-ISRS Joint Int. Workshop Earth Observat. Agricult. Monit.*, vol. 42, 2019, p. 403.

[52] P. Dash, F.-M. Göttsche, F.-S. Olesen, and H. Fischer, "Land surface temperature and emissivity estimation from passive sensor data: Theory and practice-current trends," *Int. J. Remote Sens.*, vol. 23, no. 3, pp. 2563–2594, 2002.

[53] F. Jacob *et al.*, "Modeling and inversion in thermal infrared remote sensing over vegetated land surfaces," in *Advances in Land Remote Sensing*. Dordrecht, The Netherlands: Springer, 2008, pp. 245–291.

[54] Z.-L. Li *et al.*, "Satellite-derived land surface temperature: Current status and perspectives," *Remote Sens. Environ.*, vol. 131, pp. 14–37, Apr. 2013.

[55] T. Schmugge, S. J. Hook, and C. Coll, "Recovering surface temperature and emissivity from thermal infrared multispectral data," *Remote Sens. Environ.*, vol. 65, no. 2, pp. 121–131, Aug. 1998.

[56] V. Payan and A. Royer, "Analysis of temperature emissivity separation (TES) algorithm applicability and sensitivity," *Int. J. Remote Sens.*, vol. 25, no. 1, pp. 15–37, Jan. 2004.

[57] F. Jacob *et al.*, "Reassessment of the temperature-emissivity separation from multispectral thermal infrared data: Introducing the impact of vegetation canopy by simulating the cavity effect with the SAIL-Thermique model," *Remote Sens. Environ.*, vol. 198, pp. 160–172, Sep. 2017.

[58] A. N. French, T. J. Schmugge, J. C. Ritchie, A. Hsu, F. Jacob, and K. Ogawa, "Detecting land cover change at the Jornada Experimental Range, New Mexico with ASTER emissivities," *Remote Sens. Environ.*, vol. 112, no. 4, pp. 1730–1748, Apr. 2008.

[59] A. R. Gillespie, S. Rokugawa, S. J. Hook, T. Matsunaga, and A. B. Kahle, "Temperature/emissivity separation algorithm theoretical basis document, version 2.4," NASA, Washington, DC, USA, Tech. Rep. ATBD NAS5-31372, 1999.

[60] A. R. Gillespie, E. A. Abbott, L. Gilson, G. Hulley, J. C. Jiménez-Muñoz, and J. A. Sobrino, "Residual errors in ASTER temperature and emissivity standard products AST08 and AST05," *Remote Sens. Environ.*, vol. 115, pp. 3681–3694, Dec. 2011.

[61] F.-M. Göttsche and G. C. Hulley, "Validation of six satellite-retrieved land surface emissivity products over two land cover types in a hyper-arid region," *Remote Sens. Environ.*, vol. 124, pp. 149–158, Sep. 2012.

[62] S. P. Grigsby, G. C. Hulley, D. A. Roberts, C. Scheele, S. L. Ustin, and M. M. Alsina, "Improved surface temperature estimates with MASTER/AVIRIS sensor fusion," *Remote Sens. Environ.*, vol. 167, pp. 53–63, Sep. 2015.

[63] S. J. Hook *et al.*, "HyspIRI level-2 thermal infrared (TIR) land surface temperature and emissivity algorithm theoretical basis document," Jet Propuls. Lab., Nat. Aeronaut. Space, Pasadena, CA, USA, Tech. Rep. JPL Publication 11-5, 2011.

[64] G. C. Hulley, S. J. Hook, and A. M. Baldridge, "ASTER land surface emissivity database of California and Nevada," *Geophys. Res. Lett.*, vol. 35, no. 13, pp. 1–6, 2008.

[65] G. C. Hulley, C. G. Hughes, and S. J. Hook, "Quantifying uncertainties in land surface temperature and emissivity retrievals from ASTER and MODIS thermal infrared data," *J. Geophys. Res., Atmos.*, vol. 117, no. D23, pp. 1–18, Dec. 2012.

[66] G. Hulley, S. Veraverbeke, and S. Hook, "Thermal-based techniques for land cover change detection using a new dynamic MODIS multispectral emissivity product (MOD21)," *Remote Sens. Environ.*, vol. 140, pp. 755–765, Jan. 2014.

[67] J. C. Jiménez-Muñoz, J. A. Sobrino, A. Gillespie, D. Sabol, and W. T. Gustafson, "Improved land surface emissivities over agricultural areas using ASTER NDVI," *Remote Sens. Environ.*, vol. 103, no. 4, pp. 474–487, Aug. 2006.

[68] J. C. Jiménez-Muñoz, J. A. Sobrino, C. Mattar, G. Hulley, and F.-M. Göttsche, "Temperature and emissivity separation from MSG/SEVIRI data," *IEEE Trans. Geosci. Remote Sens.*, vol. 52, no. 9, pp. 5937–5951, Sep. 2014.

[69] M. Mira, T. J. Schmugge, E. Valor, V. Caselles, and C. Coll, "Comparison of thermal infrared emissivities retrieved with the two-lid box and the TES methods with laboratory spectra," *IEEE Trans. Geosci. Remote Sens.*, vol. 47, no. 4, pp. 1012–1021, Apr. 2009.

[70] M. Mira, T. J. Schmugge, E. Valor, V. Caselles, and C. Coll, "Analysis of ASTER emissivity product over an arid area in southern New Mexico, USA," *IEEE Trans. Geosci. Remote Sens.*, vol. 49, no. 4, pp. 1316–1324, Apr. 2011.

[71] D. E. Sabol, Jr., A. R. Gillespie, E. Abbott, and G. Yamada, "Field validation of the ASTER temperature–emissivity separation algorithm," *Remote Sens. Environ.*, vol. 113, no. 11, pp. 2328–2344, Nov. 2009.

[72] T. Schmugge, A. French, J. C. Ritchie, A. Rango, and H. Pelgrum, "Temperature and emissivity separation from multispectral thermal infrared observations," *Remote Sens. Environ.*, vol. 79, nos. 2–3, pp. 189–198, 2002.

[73] J. A. Sobrino, J. C. Jiménez-Muñoz, L. Balick, A. R. Gillespie, D. A. Sabol, and W. T. Gustafson, "Accuracy of ASTER level-2 thermal-infrared standard products of an agricultural area in Spain," *Remote Sens. Environ.*, vol. 106, no. 2, pp. 146–153, Jan. 2007.

[74] J. A. Sobrino and J. C. Jiménez-Muñoz, "Minimum configuration of thermal infrared bands for land surface temperature and emissivity estimation in the context of potential future missions," *Remote Sens. Environ.*, vol. 148, pp. 158–167, May 2014.

[75] X. Zheng, Z.-L. Li, F. Nerry, and X. Zhang, "A new thermal infrared channel configuration for accurate land surface temperature retrieval from satellite data," *Remote Sens. Environ.*, vol. 231, Sep. 2019, Art. no. 111216.

[76] T. Warner, D. Levandowski, and E. Abbott, "Optimum band selection for estimating emittance," in *Proc. 2nd TIMS Workshop*, Pasadena, CA, USA, 1990, pp. 26–30.

[77] J. M. Norman and F. Becker, "Terminology in thermal infrared remote sensing of natural surfaces," *Agricult. Forest Meteorol.*, vol. 77, nos. 3–4, pp. 153–166, Dec. 1995.

[78] A. Olioso, "Simulating the relationship between thermal emissivity and the normalized difference vegetation index," *Int. J. Remote Sens.*, vol. 16, no. 16, pp. 3211–3216, Nov. 1995.

[79] A. Olioso, F. Jacob, and M. Weiss, "First evaluation of land surface emissivity spectra simulated with the sail-thermique model," in *Proc. IEEE Int. Geosci. Remote Sens. Symp. (IGARSS)*, Jul. 2018, pp. 3951–3954.

[80] F. Jacob, X. F. Gu, J.-F. Hanocq, N. Tallet, and F. Baret, "Atmospheric corrections of single broadband channel and multidirectional airborne thermal infrared data: Application to the ReSeDA experiment," *Int. J. Remote Sens.*, vol. 24, no. 16, pp. 3269–3290, Jan. 2003.

[81] J. C. Jiménez-Muñoz and J. A. Sobrino, "Error sources on the land surface temperature retrieved from thermal infrared single channel remote sensing data," *Int. J. Remote Sens.*, vol. 27, nos. 5–6, pp. 999–1014, Mar. 2006.

[82] L. Labarre *et al.*, "An overview of MATISSE-v2.0," *Proc. SPIE*, vol. 7828, Oct. 2010, Art. no. 782802.

[83] L. Labarre *et al.*, "MATISSE-v2.0: New functionalities and comparison with MODIS satellite images," *Proc. SPIE*, vol. 8014, May 2011, Art. no. 80140Z.

[84] J. A. Barsi, J. L. Barker, and J. R. Schott, "An atmospheric correction parameter calculator for a single thermal band Earth-sensing instrument," in *Proc. IEEE Int. Geosci. Remote Sens. Symp. (IGARSS)*, vol. 5, Jul. 2003, pp. 3014–3016.

[85] F. Palluconi, G. Hoover, R. Alley, M. Jentoft-Nilsen, and T. Thompson, "An atmospheric correction method for aster thermal radiometry over land," ASTER ATBD Revision 3, Jet Propuls. Lab., Pasadena, CA, USA, Tech. Rep., 1999.

[86] R Foundation for Statistical Computing, Austria. (2011). *R Core Team: R: A Language and Environment for Statistical Computing*. [Online]. Available: http://www.R-project.org/

[87] R. Fletcher and C. M. Reeves, "Function minimization by conjugate gradients," *Comput. J.*, vol. 7, no. 2, pp. 149–154, 1964.

[88] G. Girouard, A. Bannari, A. El Harti, and A. Desrochers, "Validated spectral angle mapper algorithm for geological mapping: Comparative study between QuickBird and Landsat-TM," in *Proc. 20th ISPRS Congr., Geo-Imag. Bridging Continents*, Istanbul, Turkey, 2004, pp. 12–23.

[89] G. P. Anderson, S. A. Clough, F. Kneizys, J. H. Chetwynd, and E. P. Shettle, "AFGL atmospheric constituent profiles (0.120 km)," Air Force Geophys. Lab., Hanscom AFB, MA, USA, Environ. Res. Paper AFGL-TR-86-0110, 954, 1986.

[90] P. Simoneau *et al.*, "MATISSE: Version 1.2 et développements futurs," in *Proc. Int. Symp. OPTRO*, Paris, France, May 2005, pp. 1–10.

[91] F. Chevallier, A. Chédin, F. Chéruy, and J.-J. Morcrette, "TIGR-like atmospheric-profile databases for accurate radiative-flux computation," *Quart. J. Roy. Meteorol. Soc.*, vol. 126, no. 563, pp. 777–785, Jan. 2000.

[92] E. Rubio, V. Caselles, and C. Badenas, "Emissivity measurements of several soils and vegetation types in the 8–14, $\mu$m wave band: Analysis of two field methods," *Remote Sens. Environ.*, vol. 59, no. 3, pp. 490–521, 1997.

[93] H. Tonooka, F. D. Palluconi, S. J. Hook, and T. Matsunaga, "Vicarious calibration of ASTER thermal infrared bands," *IEEE Trans. Geosci. Remote Sens.*, vol. 43, no. 12, pp. 2733–2746, Dec. 2005.

[94] J. C. Jiménez-Muñoz and J. A. Sobrino, "Emissitivity spectra obtained from field and laboratory measurements using the temperature and emissivity separation algorithm," *Appl. Opt.*, vol. 45, no. 27, pp. 7104–7109, 2006.

[95] H. Fujisada, "Design and performance of aster instrument," *Proc. SPIE*, vol. 2583, pp. 16–25, Dec. 1995.

[96] C. Coll *et al.*, "Temperature and emissivity separation from ASTER data for low spectral contrast surfaces," *Remote Sens. Environ.*, vol. 110, no. 2, pp. 162–175, 2007.

[97] J. Gomis-Cebolla, J. C. Jimenez, and J. A. Sobrino, "LST retrieval algorithm adapted to the Amazon evergreen forests using MODIS data," *Remote Sens. Environ.*, vol. 204, pp. 401–411, Jan. 2018.